State of charge estimation for lithium-ion battery based on an intelligent adaptive unscented Kalman filter

Sun, D., Yu, X., Zhang, C., Wang, C. & Huang, R.

Original citation & hyperlink:
Sun, D, Yu, X, Zhang, C, Wang, C & Huang, R 2020, 'State of charge estimation for lithium-ion battery based on an intelligent adaptive unscented Kalman filter', International Journal of Energy Research, vol. 44, no. 14, pp. 11199-11218. https://dx.doi.org/10.1002/er.5690

DOI 10.1002/er.5690
ISSN 0363-907X
ESSN 1099-114X

Publisher: Wiley

State of Charge Estimation for Lithium-Ion Battery based on an Intelligent Adaptive Unscented Kalman Filter

Daoming Sun[a], Xiaoli Yu[a]*, Cheng Zhang[b], Chongming Wang[b], Rui Huang[a]

[a] *Department of Energy Engineering, Zhejiang University, Hangzhou 310027, China*

[b] *Centre for Advanced Low Carbon Propulsion Systems, Coventry University, Coventry, United Kingdom, CV1 5FB*

* Corresponding author *E-mail address:* yuxl@zju.edu.cn; (Prof X. Yu)

Abstract: Adaptive unscented Kalman filter (AUKF) has been widely used for state of charge (SOC) estimation of lithium-ion battery. The noise covariance of the conventional AUKF method is updated based on the innovation covariance matrix (ICM), which is estimated using the error innovation sequence (EIS). However, the distribution of EIS changes due to the time-varying noise, load current dynamics and modelling error, which will lead to inaccurate ICM estimation. Therefore, an intelligent adaptive unscented Kalman filter (IAUKF) method is proposed to detect the distribution change of EIS. Then, the ICM is estimated based on the EIS after the distribution change. Results show that the IAUKF method can improve SOC estimation accuracy significantly. Compared to that of the AUKF method, the Root Mean Squared Error (RMSE) and the Mean Absolute Error (MAE) of SOC based on the IAUKF method decrease by 43.70% and 72.37% under random walk discharge condition, respectively. In addition, the computation time of the IAUKF method slightly increases by 6.27% compared with that of AUKF method. Finally, the effect of initial parameters on the SOC estimation accuracy was analysed. The results indicate that proper algorithm tuning, such as initial window length of EIS for ICM update and the threshold value, can further improve the SOC accuracy based on the proposed IAUKF method. The proposed IAUKF method also shows high robustness against initial measurement noise covariance.

Keywords: Lithium-ion battery; State of Charge; Error innovation sequence; Distribution change; Intelligent adaptive unscented Kalman filter

Abbreviation

AEKF: Adaptive EKF
AUKF: Adaptive UKF
APF: Adaptive PF
AHIF: Adaptive H infinity filter
DEKF: Dual EKF
DHIF: Dual H infinity filter
DUKF: Dual UKF
ECM: Equivalent circuit model
EIS: Error innovation sequence
EKF: Extended Kalman filter
ICM: Innovation covariance matrix
IAUKF: Intelligent AUKF
LIBs: Lithium-ion batteries
MAE: Mean absolute error
ML: Maximum likelihood
OCV: Open circuit voltage
PDF: Probability density function
PF: Particle filter
RLS: Recursive least square
RMSE: Root mean squared error
ST-UKF: Strong tracking-UKF
UKF: Unscented Kalman filter

1. Introduction

Lithium-ion batteries (LIBs) are widely used in various fields because of its long lifespan, high energy density and low self-discharge rate [1, 2]. Electric vehicles are one of the typical applications for LIBs [3]. The state of charge (SOC) is one of the core indicators of LIBs that must be monitored online [4]. The LIBs may suffer from the risk of over-discharge or over-charge if the SOC is estimated inaccurately [5]. The lifetime of LIBs will be shortened as a result of over-discharge or over-charge. In extreme cases, over-charge may lead to thermal runaway of LIBs. Therefore, improvement of SOC estimation accuracy is crucial for safe use and long life of LIBs.

A lot of SOC estimation methods have been proposed for LIBs. These methods can be classified into four categories. The first category is the coulomb counting method [6]. This method is easy to implement by integrating the current over time. However, accurate prior information on the initial SOC must be provided for coulomb counting method. Further, coulomb counting method is an open loop method and lacks the ability of feedback correction [7]. As a result, coulomb counting method is vulnerable to electric current measurement errors, especially the bias error. The second one is the open-circuit voltage (OCV) method [8]. In the OCV method, the relationship between SOC and OCV is built using the OCV test data. However, it takes long time for the LIBs to reach equilibrium state due to the slow internal diffusion dynamics [9]. The third one is the data-driven methods [10]. Typical data-driven methods include neural networks [11-13], support vector regression [14] and fuzzy system [15]. The data-driven methods are capable of self-learning from data. Complicated knowledge of electrochemical dynamics is not necessary for the data-driven methods. However, substantial data is indispensable for the data-driven methods, which requires long test time. Careful experimental test design is also needed as the model performance depends on the quality of the training data set. The last one is model-based methods [16, 17]. The model-based method is the fusion of battery model and state estimation algorithm. This is a closed-loop SOC estimation method,

and has proved to be accurate and implementable online due to the low complexity. In comparison with the coulomb counting and OCV-based methods, model-based methods are capable of feedback state correction [11]. Compared with data-driven methods, model-based methods do not require substantial data for model training [12].

Due to the advantages mentioned above, the model-based methods become the research hotspot in the field of SOC estimation [18-20]. The model-based method is a combination of battery model, parameter identification algorithm and filter algorithm. Electrochemical model [21, 22] and equivalent circuit model (ECM) [23] are two kinds of battery models widely used for describing the characteristics of LIBs. For online SOC estimation, ECM is widely used because of a good balance between computation complexity and estimation accuracy. Thevenin model is one of the typical ECMs used for the SOC estimation [24, 25]. It consists of an OCV, an internal resistor and a RC network. Different ways have been proposed to describe the OCV-SOC relationship, such as polynomial function, logarithmic function and exponential function [26]. With the obtained OCV model, the other parameters in the ECM can be identified from experimental data. Parameter identification methods can be classified into two categories: 1) offline identification method; 2) online identification method. Genetic algorithm [27], Particle swarm algorithm [28] and simulated annealing algorithm [29] are widely used for offline identification of ECM parameters. However, the parameters of ECM are time-varying during the charging/discharging operation. Therefore, online identification methods, such as recursive least square (RLS) method, are proposed for improved accuracy of parameter identification in this paper. Once the parameters of LIBs are identified online, the SOC of LIBs can be estimated based on various kinds of filter algorithms. Among these filter algorithms, extended Kalman filter (EKF) [17, 30-32], unscented Kalman filter (UKF) [33, 34], cubature Kalman filter (CKF) [24, 35, 36] and particle filter (PF) [10] are the popular state filter algorithms used for SOC estimation. The filter performance depends on careful selection of the

tuning parameters, such as the ICM [37]. Under real-world operation conditions the noise characteristics may change because of change of performance of sensors and environment. For example, the measurement error of the electric current sensor depends on the current magnitude. However, in these algorithms, the update of covariance of measurement and process noise are neglected.

To cope with such problems, a lot of adaptive filters have been proposed to update the noise covariance to improve SOC estimation accuracy. Commonly used adaptive filters include the adaptive EKF (AEKF) [13], adaptive UKF (AUKF) [14][33], adaptive H infinity filter (AHIF) [38], and adaptive PF (APF) [28]. Apart from these adaptive filter algorithms, a lot of dual-filters were proposed for simultaneous parameter and state estimation of LIBs. Dual-filters are made of two filters. One is used for the parameter identification, and the other for the SOC estimation. Typical dual-filters, such as dual EKFs (DEKF) [39, 40], dual UKF (DUKF) [41, 42] and dual HIF (DHIF) [43], were proposed for the SOC estimation. In comparison with filters based on offline-identified parameters, the dual filters can achieve better SOC estimation accuracy. Considering that the change rate of parameters and state of LIBs may be different during operation, multi-time scale dual filters, such as multi-time scale DEKF [44], were proposed. For example, for slow-changing parameter, such as capacity, the updating rate is relatively low. In the comparison of dual filters, multi-time scale dual filters can achieve similar accuracy with less computation time. In order to update the covariance of measurement noise, double adaptive filters, such as multi-time scale dual AEKF [8] and multi-time scale dual adaptive PF [45], were proposed for the parameter and state estimation. Compared with multi-time scale dual filters, the multi-time scale dual adaptive ones can improve the SOC estimation accuracy by online adaption of the measurement noise covariance.

Despite of these improvements, the distribution change of the EIS was neglected in these filters, which may lead to inaccurate ICM estimation. In the existing AUKF method, the ICM is updated

based on fixed-length EIS, and the distribution change of EIS is not detected. However, several causes can lead to the change of the EIS distribution under dynamic load profiles. First, the measurement error of the current/voltage sensors depends on the signal amplitude. Second, the battery model error depends on the operating condition. For example, the battery model can achieve high accuracy when the real-time load current profile matches the data set used for model parameterization. In contrast, the model error can increase under a very different load profile. Before and after the border of distribution change of EIS, the ICMs are different. This effect is neglected in the existing adaptive SOC filter algorithms which generally update EIS covariance using a fixed-length window. As a result, it leads to inaccurate ICM estimation, which reduces the SOC estimation accuracy.

The key contribution of this paper is that an intelligent adaptive Unscented Kalman filter (IAUKF) is proposed for accurate SOC estimation. First, the EIS distribution change is detected based on maximum likelihood. Second, the ICM is estimated with the EIS after that change point. The purpose of improving SOC estimation accuracy with intelligent noise estimator is achieved.

The outline of the paper is as follows: The battery model and parameter identification is presented in Section 2. In Section 3, the IAUKF method is introduced. Section 4 presents the experimental results and analysis. Conclusions are given in Section 5.

2 Introduction of Battery Model and Parameter Identification

2.1 Description of Lithium-ion Battery Model

The battery model must be established before the SOC estimation. Thevenin model is widely used for the SOC estimation as a good trade-off between complexity and accuracy [46]. As shown in Fig. 1, Thevenin model consists of a voltage source U_{oc}, a series-connected ohmic resistor R_s, and an RC network (R_p and C_p).

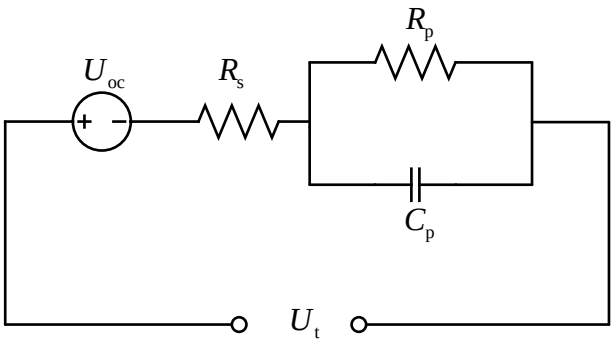

Fig. 1. Thevenin model

According to Kirchhoff voltage laws and Kirchhoff's current law, the Thevenin model equation can be obtained as follows

$$\begin{cases} \dot{U}_p = \dfrac{i}{C_p} - \dfrac{U_p}{C_p \cdot R_p} \\ U_t = U_{oc} - U_p - i \cdot R_s \end{cases} \tag{1}$$

where U_p is the polarization voltage, U_t is the terminal voltage. i is the load current with a positive value for discharge and a negative value for charge. U_{oc} is the OCV, and a polynomial is used here to describe the OCV-SOC relationship, as $U_{oc}(\mathrm{SOC}) = K_0 + K_1 \cdot \mathrm{SOC} + K_2 \cdot \mathrm{SOC}^2 + \ldots + K_n \cdot \mathrm{SOC}^n$.

Discretising Eq. (1) and adding the state variable SOC, the model equations become

State equation:
$$\begin{cases} U_{p,k} = \exp\left(-\dfrac{\Delta t}{C_{p,k-1} R_{p,k-1}}\right) \cdot U_{p,k-1} + \left(1 - \exp\left(-\dfrac{\Delta t}{C_{p,k-1} R_{p,k-1}}\right)\right) \cdot R_{p,k-1} i_{k-1} \\ \mathrm{SOC}_k = \mathrm{SOC}_{k-1} - \dfrac{\eta \cdot i_{k-1} \cdot \Delta t}{3600 \cdot \mathrm{C_n}} \end{cases} \tag{2}$$

Measurement equation:
$$U_{t,k} = U_{oc,k} - U_{p,k} - i_k \cdot R_{s,k} \tag{3}$$

where $U_{p,k}$, $U_{oc,k}$ and $U_{t,k}$ represent the polarization voltage, OCV and terminal voltage at time step k, respectively. i_{k-1} represents the load current at the time step $k-1$. SOC_k represents the SOC at the time step k. η is the charge and discharge efficiency of the LIBs. Δt is the sampling time interval. $\mathrm{C_n}$ represents the nominal capacity of the battery.

Eq. (2) and (3) can be reformulated as follows considering the noises

$$\begin{cases} \mathbf{x}_k = \mathbf{A}_{k-1}\mathbf{x}_{k-1} + \mathbf{B}_{k-1}\mathbf{u}_{k-1} + \mathbf{w}_k \\ \mathbf{y}_k = g\left(\mathbf{x}_k, \mathbf{u}_k\right) + \upsilon_k \end{cases} \tag{4}$$

where $\mathbf{x}_k = \begin{bmatrix} U_{\mathrm{p},k} \\ \mathrm{SOC}_k \end{bmatrix}$, $\mathbf{A}_{k-1} = \begin{bmatrix} \exp\left(-\dfrac{\Delta t}{C_{\mathrm{p},k-1}R_{\mathrm{p},k-1}}\right) & 0 \\ 0 & 1 \end{bmatrix}$, $\mathbf{B}_{k-1} = \begin{bmatrix} \left(1-\exp\left(-\dfrac{\Delta t}{C_{\mathrm{p},k-1}R_{\mathrm{p},k-1}}\right)\right)\cdot R_{\mathrm{p},k-1} \\ \dfrac{\eta\cdot\Delta t}{3600\cdot \mathrm{C_n}} \end{bmatrix}$, $\mathbf{u}_k = i_k$,

$\mathbf{y}_k = U_{\mathrm{t},k}$, $g\left(\mathbf{x}_k, \mathbf{u}_k\right) = U_{\mathrm{oc},k} - U_{\mathrm{p},k} - i_k \cdot R_{\mathrm{s},k}$. $\mathbf{w}_k$ and υ_k are the process noise and measurement noise, respectively.

2.2 Parameter identification for ECM

In order to improve the accuracy of online parameter identification, the initial parameters must be set properly. Based on the OCV tests, a set of data points ($\mathrm{SOC}, \mathrm{OCV}$) are obtained. Then, the coefficients ($K_0, K_1, K_2, \ldots, K_n$) in the OCV model are obtained by fitting these points. With the obtained OCV model, the initial parameter values ($R_\mathrm{s}, R_\mathrm{p}, C_\mathrm{p}$) of the ECM can be estimated by minimizing the objective function in Eq. (5), using the GA algorithm.

$$\begin{aligned} &\text{find: } R_\mathrm{s}, R_\mathrm{p}, C_\mathrm{p} \\ &\min\ f\left(R_\mathrm{s}, R_\mathrm{p}, C_\mathrm{p}\right) = \sum_{k=1}^{N_\mathrm{pds}} \left(U_{\mathrm{t},k}\left(t\right) - U_{\mathrm{t},k}^{\ *}\left(t\right)\right)^2 \\ &\text{s.t.}\quad R_\mathrm{s} > 0, R_\mathrm{p} > 0, C_\mathrm{p} > 0 \end{aligned} \tag{5}$$

where $U_{\mathrm{t},k}^{\ *}\left(t\right)$ is the measured terminal voltage, N_pds is the length of test data.

As the parameters of the ECM change during the operation condition, the parameters ($R_\mathrm{s}, R_\mathrm{p}, C_\mathrm{p}$) of the ECM need to be identified online. Taking both complexity and accuracy into consideration, forgetting factor-RLS (FF-RLS) is adopted for online parameter identification. The initial parameters required for FF-RLS are set to the values obtained above. The detailed implementation process of FF-RLS algorithm can be found in Ref. [47].

3 IAUKF for SOC estimation

3.1 AUKF algorithm

In the AUKF method, the measurement and process noise covariance are updated online based on the covariance matching principle. The AUKF method has been widely used for the state estimation of nonlinear systems. It consists of three parts: model prediction step, state correction step and covariance matching. The state and measurement equations used in the AUKF method are usually expressed as follows:

$$\begin{cases} \mathbf{x}_k = f\left(\mathbf{x}_{k-1}, \mathbf{u}_{k-1}\right) + \mathbf{w}_k \\ \mathbf{y}_k = g\left(\mathbf{x}_k, \mathbf{u}_k\right) + \boldsymbol{\upsilon}_k \end{cases} \tag{6}$$

where $\mathbf{x}_k$ is the system state vector, $\mathbf{y}_k$ is the measurement vector, $\mathbf{u}_k$ is the known input vector, $\mathbf{w}_k$ is the process Gaussian noise, $\boldsymbol{\upsilon}_k$ is the measurement Gaussian noise, $f\left(\mathbf{x}_k, \mathbf{u}_k\right)$ is a nonlinear state function, and $g\left(\mathbf{x}_k, \mathbf{u}_k\right)$ is a nonlinear measurement function.

The detailed algorithm of AUKF [48] is as follows:

Model prediction step

(1) Initialization

$$\hat{\mathbf{x}}_{0|0} = E\left[\mathbf{x}_0\right], \quad \mathbf{P}_{xx,0|0} = E\left[\left(\mathbf{x}_0 - \hat{\mathbf{x}}_0\right)\left(\mathbf{x}_0 - \hat{\mathbf{x}}_0\right)^{\mathrm{T}}\right], \quad \mathbf{R}_0, \quad \mathbf{Q}_0 \tag{7}$$

where $\mathbf{R}_0$ and $\mathbf{Q}_0$ are initial measurement and process noise covariance.

(2) Computing the sigma points

$$\hat{\mathbf{x}}^{(i)}_{k-1|k-1} = \hat{\mathbf{x}}_{k-1|k-1}, i = 0 \tag{8}$$

$$\hat{\mathbf{x}}^{(i)}_{k-1|k-1} = \hat{\mathbf{x}}_{k-1|k-1} + \sqrt{\left(n+\lambda\right)\mathbf{P}_{xx,k-1|k-1}}, i = 1, \ldots, n \tag{9}$$

$$\overset{\wedge(i)}{\mathbf{x}}_{k-1|k-1} = \overset{\wedge}{\mathbf{x}}_{k-1|k-1} - \sqrt{(n+\lambda)\mathbf{P}_{xx,k-1|k-1}}, i = n+1,\ldots,2n \tag{10}$$

where λ denotes a scaling factor, and

$$\lambda = \alpha^2(n+k_a) - n \tag{11}$$

α determines the spread of the sigma points around the mean state value. k_a is the second scaling parameter that is usually set to 0. Smaller value k_a corresponds to sigma points closer to the mean state. The spread is proportional to the square-root of k_a.

(3) Time update

$$\overset{\wedge(i)}{\mathbf{x}}_{k|k-1} = f\left(\overset{\wedge(i)}{\mathbf{x}}_{k-1|k-1}, \mathbf{u}_{k-1}\right) \tag{12}$$

$$\overset{\wedge}{\mathbf{x}}_{k|k-1} = \sum_{i=0}^{2n} \omega_m^i \overset{\wedge(i)}{\mathbf{x}}_{k-1|k-1} \tag{13}$$

where $\omega_m^0 = \dfrac{\lambda}{n+\lambda}$, $\omega_m^i = \dfrac{1}{2(n+\lambda)}$, $i = 1,\ldots,2n$.

$$\overset{\wedge}{\mathbf{P}}_{xx,k|k-1} = \sum_{i=0}^{2n} \omega_c^i \left(\overset{\wedge(i)}{\mathbf{x}}_{k|k-1} - \overset{\wedge}{\mathbf{x}}_{k|k-1}\right)\left(\overset{\wedge(i)}{\mathbf{x}}_{k|k-1} - \overset{\wedge}{\mathbf{x}}_{k|k-1}\right)^{\mathrm{T}} + \mathbf{Q}_k \tag{14}$$

where $\omega_c^0 = \dfrac{\lambda}{\lambda+n} + \left(1-\alpha^2+\beta\right)$, $\omega_c^i = \dfrac{1}{2(n+\lambda)}, i = 1,\ldots,2n$. β represents the prior knowledge of the state distribution. For Gaussian distributions, $\beta = 2$.

State correction step

(4) Measurement update

$$\overset{\wedge(i)}{\mathbf{y}}_{k|k-1} = g\left(\overset{\wedge(i)}{\mathbf{x}}_{k|k-1}, u_k\right) \tag{15}$$

$$\hat{\mathbf{y}}_{k|k-1} = \sum_{i=0}^{2n} \omega_m^i \hat{\mathbf{y}}_{k|k-1}^{(i)} \tag{16}$$

$$\mathbf{P}_{yy,k|k-1} = \sum_{i=0}^{2n} \omega_c^i \left(\hat{\mathbf{y}}_{k|k-1}^{(i)} - \hat{\mathbf{y}}_{k|k-1} \right) \left(\hat{\mathbf{y}}_{k|k-1}^{(i)} - \hat{\mathbf{y}}_{k|k-1} \right)^{\mathrm{T}} + \mathbf{R}_k \tag{17}$$

$$\mathbf{P}_{xy,k|k-1} = \sum_{i=0}^{2n} \omega_c^i \left(\hat{\mathbf{x}}_{k|k-1}^{(i)} - \hat{\mathbf{x}}_{k|k-1} \right) \left(\hat{\mathbf{y}}_{k|k-1}^{(i)} - \hat{\mathbf{y}}_{k|k-1} \right)^{\mathrm{T}} \tag{18}$$

(5) Measurement correction

$$\mathbf{K}_k = \mathbf{P}_{xy,k|k-1} \mathbf{P}_{yy,k|k-1}^{-1} \tag{19}$$

$$\mathbf{e}_k = \mathbf{y}_k - \hat{\mathbf{y}}_{k|k-1} \tag{20}$$

$$\hat{\mathbf{x}}_{k|k} = \hat{\mathbf{x}}_{k|k-1} + \mathbf{K}_k \mathbf{e}_k \tag{21}$$

$$\mathbf{P}_{xx,k|k} = \mathbf{P}_{xx,k|k-1} - \mathbf{K}_k \mathbf{P}_{yy,k|k-1} \mathbf{K}_k^{\mathrm{T}} \tag{22}$$

Covariance matching

(6) Process and measurement noise covariance update

$$\mathbf{H}_k = \frac{1}{M} \sum_{i=k-M+1}^{k} \mathbf{e}_k \mathbf{e}_k^{\mathrm{T}} \tag{23}$$

$$\mathbf{R}_k = \mathbf{H}_k - \mathbf{C}_k \mathbf{P}_{xx,k|k-1} \mathbf{C}_k^{\mathrm{T}} \tag{24}$$

$$\mathbf{Q}_k = \mathbf{K}_k \mathbf{H}_k \mathbf{K}_k^{\mathrm{T}} \tag{25}$$

where $\mathbf{C}_k = \left. \frac{\partial g(\mathbf{x}, \mathbf{u}_k)}{\partial \mathbf{x}} \right|_{\mathbf{x} = \hat{\mathbf{x}}_{k|k-1}}$. M is the fixed window length.

The ICM $\mathbf{H}_k$ is updated online based on Eq. (23). Then the noise covariance $\mathbf{R}_k$ and $\mathbf{Q}_k$ are updated based on Eq. (24) and (25) in the AUKF algorithm. When the AUKF algorithm is applied for

SOC estimation of LIBs, $f\left(\begin{matrix}\wedge(i)\\ \mathbf{x}_{k-1|k-1},\mathbf{u}_{k-1}\end{matrix}\right)$ in Eq. (12) can be substituted by the state equation of battery model in Eq. (4).

3.2 Intelligent noise estimator

3.2.1 Detection of the distribution change of the EIS

In the AUKF algorithm, the ICM is estimated based on the fixed length (M) EIS according to Eq. (23). However, the EIS is affected by both load current dynamics and battery model error. The distribution of EIS may change during the charge and discharge process. In order to accurately estimate ICM, the border of distribution change of EIS need to be detected. Then the EIS after that border can be used for updating the ICM estimation. An intelligent approach is proposed here to detect the border of distribution change of the EIS.

A detection window with length $2N$ is considered. The EIS within this window is expressed as $[e_{k-2N},e_{k-2N+1},\ldots,e_{k-1}]$, where e_k is the EIS at the time step k in Eq. (20). If the EIS follows a white Gaussian noise distribution, the mean and variance of the EIS inside the detection window are zero and σ^2 respectively. The probability density function (PDF) of this EIS inside the detection window can be expressed as follows:

$$f(e_k)=\frac{1}{\sqrt{2\pi\sigma^2}}e^{-\frac{e_k^2}{2\sigma^2}},e_k\sim N\left(0,\sigma^2\right) \tag{26}$$

At each sampling step k, a new error innovation e_k will pop into the detection window. If the EIS distribution changes slowly, the PDF of the EIS within the new detection window will remain almost the same as before, and the ICM $\mathbf{H}_k$ can be estimated using Eq. (23). Because the estimation accuracy of ICM increases with the window length, the new error innovation can be added to the detection window for covariance estimation. However, if the distribution of the EIS changes rapidly, the EIS in the new detection window may follow two different PDFs and the ICM can't be estimated

accurately using Eq. (23). It is then required to detect the border of the distribution change of the EIS inside the detection window. Once this border is detected, the EIS received after the border will be used to estimate the new ICM. The window length of the EIS used for ICM estimation will be reset. Therefore, the window length increases between two borders of distribution change and is reset once the new border of distribution change arrives.

The values of EIS can be either positive or negative. However, the amplitude of EIS variation is equal when the square of the EIS is the same. Therefore, in this paper, the border of distribution change of EIS is detected based on the square of the EIS. Let $Z_k = e_k^2$, then cumulative distribution function of Z_k can be obtained as the following equation,

$$F_{Z_k}(z_k) = P\left(-\sqrt{z_k} \le e_k \le \sqrt{z_k}\right) = F\left(\sqrt{z_k}\right) - F\left(-\sqrt{z_k}\right) \tag{27}$$

The PDF of Z_k can be obtained by differentiating both sides of Eq. (27) as follows:

$$f_{Z_k}(z_k) = \frac{1}{2\sqrt{z_k}}\left(f\left(\sqrt{z_k}\right) + f\left(-\sqrt{z_k}\right)\right) = \frac{1}{\sqrt{2\pi\sigma^2 z_k}} e^{-\frac{z_k}{2\sigma^2}} \tag{28}$$

The variance of the EIS inside the detection window can be estimated based on the Maximum-Likelihood (ML) method. If the sequence Z inside the detection window is given as $Z = [Z_{k-2N}, \ldots, Z_{k-N}, \ldots, Z_{k-1}]$, since the data of the sequence Z are independent, the PDF of the sequence Z equals the product of the individual sequence data.

$$f_Z(z) = \prod_{n=k-2N}^{k-1} \frac{1}{\sqrt{2\pi\sigma^2 z_n}} e^{-\frac{z_n}{2\sigma^2}} \tag{29}$$

where $Z = [z_{k-2N}, \ldots, z_{k-N}, \ldots, z_{k-1}]$. In order to obtain the variance σ^2 based on ML estimation $\ln\left(f_Z(z)\right)$ must be maximised. From Eq. (29), we can get

$$\ln\left(f_Z(z)\right) = -\frac{1}{2}\sum_{n=k-2N}^{k-1}\left[\ln\left(2\pi\sigma^2 z_n\right) + \frac{z_n}{\sigma^2}\right] \tag{30}$$

Let $\frac{\partial \ln\left(f_Z(z)\right)}{\partial \sigma^2}=0$, then σ^2 can be obtained as follows

$$\sigma^2=\frac{1}{2N}\sum_{n=k-2N}^{k-1} z_n \tag{31}$$

Substitute Eq. (31) into Eq. (30), we can obtain the logarithmic ML function value ML_1, as shown in Eq. (32)

$$\begin{aligned} ML_1 &= \max\left(\ln\left(f_Z(z)\right)\right) \\ &= -\frac{1}{2}\sum_{n=k-2N}^{k-1}\left[\ln\left(2\pi\sigma^2 z_n\right)+\frac{z_n}{\sigma^2}\right] \end{aligned} \tag{32}$$

In order to detect the border of the distribution change of the EIS, the distribution change point inside the detection window must be checked at each time step. The initial window length is set to L_0, where $L_0=2N$. The indexes of points in the first half of the detection window start from 1 to N. The indexes of points in the second half of the detection window begin from $N+1$ to $2N$. According to the previous analysis, the length of the detection window increases if there is no distribution change of the EIS. Then, the location of the middle point in the detection window also changes with the increasing window length. Assume that there is a distribution change after the middle point in the detection window, then the first and second half of the detection window follow two different distributions, the PDF of the EIS in the whole detection window equals the product of the PDFs in two regions:

$$f_Z(z)=\prod_{n=k-N}^{k-1}\frac{1}{\sqrt{2\pi\sigma_1^2 z_n}}e^{-\frac{z_n}{2\sigma_1^2}}\prod_{n=k-2N}^{k-N-1}\frac{1}{\sqrt{2\pi\sigma_2^2 z_n}}e^{-\frac{z_n}{2\sigma_2^2}} \tag{33}$$

where the sequences in the first and second half of the detection window follow Gaussian distribution with variance σ_1^2 and σ_2^2, respectively. From Eq. (33)

$$\ln\left(f_Z(z)\right)=-\frac{1}{2}\sum_{n=k-N}^{k-1}\left[\ln\left(2\pi\sigma_1^2 z_n\right)+\frac{z_n}{\sigma_1^2}\right]-\frac{1}{2}\sum_{n=k-2N}^{k-N-1}\left[\ln\left(2\pi\sigma_2^2 z_n\right)+\frac{z_n}{\sigma_2^2}\right] \tag{34}$$

Let $\frac{\partial \ln\left(f_Z(z)\right)}{\partial \sigma_1^2}=0$ and $\frac{\partial \ln\left(f_Z(z)\right)}{\partial \sigma_2^2}=0$, σ_1^2 and σ_2^2 can be computed as follows:

$$\sigma_1^2=\frac{1}{N}\sum_{n=k-N}^{k-1} z_n \tag{35}$$

$$\sigma_2^2=\frac{1}{N}\sum_{n=k-2N}^{k-N-1} z_n \tag{36}$$

Substitute Eq. (35) and Eq. (36) into Eq. (34), we can obtain the logarithmic ML function value ML_2 under the conditions of the distribution change of the EIS, as shown in Eq. (37):

$$\begin{aligned} ML_2 &= \max\left(\ln\left(f_Z(z)\right)\right) \\ &= -\frac{1}{2}\sum_{n=k-N}^{k-1}\left[\ln\left(2\pi\sigma_1^2 z_n\right)+\frac{z_n}{\sigma_1^2}\right]-\frac{1}{2}\sum_{n=k-2N}^{k-N-1}\left[\ln\left(2\pi\sigma_2^2 z_n\right)+\frac{z_n}{\sigma_2^2}\right] \end{aligned} \tag{37}$$

Next, ML_1 and ML_2 can be used for detection of distribution change. If there exists a border of the distribution change of the EIS within the detection window, the value ML_2 will be greater than ML_1; Otherwise, the opposite is true. Therefore, the border of the distribution change of the EIS can be detected according to Eq. (38). The parameter Th in Eq. (38) is the threshold value that can be set through trial and error.

$$ML_2 - ML_1 > Th \tag{38}$$

If Th is too large, the chance of detection of the border of the distribution change of the EIS becomes small. Conversely, if Th is too small, even slight variation in the distribution change of the EIS can lead to a false alarm. It is found that $Th=N$ is a proper choice through trial and error. Next, Eq. (38) must be checked at each time step. If this condition is met, the distribution change of the EIS is detected, and the EIS received prior to detected border can't be used for estimating the ICM after the detected border.

The initial window length L_0 is $2N$. If no distribution change of the EIS is detected, detection window length will increase. The computation load of the detection algorithm will increase when the

estimation window length increases. Therefore, a maximum value $L_{\max}$ should be set for the window length to limit the computation expense. In view of this, an adaptive window length is described as follows

$$\begin{aligned}
&\text{Initialization}\\
&\quad L_0 = 2N;\\
&\text{For step } k = 1,2,\ldots,\\
&\quad L_k = L_{k-1} + 1; \quad \text{if } ML_2 - ML_1 < Th \text{ and } L_{k-1} < L_{\max}\\
&\quad L_k = L_{\max}; \quad \text{if } ML_2 - ML_1 < Th \text{ and } L_{k-1} = L_{\max}\\
&\quad L_k = 2N; \quad \text{if } ML_2 - ML_1 > Th
\end{aligned} \tag{39}$$

In order to reduce computational complexity, Eq. (32) and (37) are simplified as follows:

$$ML_1 = -\frac{1}{2}\left[2N\ln(2\pi) + 2N\ln(\sigma^2) + \sum_{n=k-2N}^{k-1}\ln(z_n) + 2N\right] \tag{40}$$

$$\begin{aligned}
ML_2 = &-\frac{1}{2}\left[N\ln(2\pi) + N\ln(\sigma_1^2) + \sum_{n=k-N}^{k-1}\ln(z_n) + N\right]\\
&-\frac{1}{2}\left[N\ln(2\pi) + N\ln(\sigma_2^2) + \sum_{n=k-2N}^{k-N-1}\ln(z_n) + N\right]
\end{aligned} \tag{41}$$

Thus, $ML_2 - ML_1$ can be simplified as follows

$$ML_2 - ML_1 = N \cdot \ln\left(\frac{\sigma^2}{\sigma_1\sigma_2}\right) \tag{42}$$

Three parameters (σ, σ_1 and σ_2) are from Eq. (31), Eq.(35) and Eq.(36), respectively. As such, the calculation of ($ML_2 - ML_1$) based on Eq. (42) is relatively simple. Then, it is easy to judge whether the condition relation described by Eq. (38) is met.

3.2.2 Noise estimator based on the selected EIS

Based on the detection method of the distribution change of the EIS, the EIS after that border can be selected to estimate the ICM. The ICM $\mathbf{H}_k$ in Eq. (23) can be estimated as follows:

$$\mathbf{H}_k = \frac{1}{L_k}\sum_{i=k-L_k+1}^{k}\mathbf{e}_k\mathbf{e}_k^{\mathrm{T}} \tag{43}$$

where L_k follows the adaptive rule described by Eq. (39).

With the obtained ICM $\mathbf{H}_k$, the covariance of the measurement $\mathbf{R}_k$ and process noise $\mathbf{Q}_k$ can be updated according to Eq. (24) and (25).

3.3 Framework of the IAUKF algorithm

The flow chart of the IAUKF-based SOC estimation is given in Fig. 2. It consists of two steps, the detection of the distribution change, and the update of the ICM. The estimation window length of the EIS is adaptive based on the detection results, as shown in the light blue part of Fig. 2. If the time step meets the condition relation $k \le L_0$, the initial measurement noise covariance $\mathbf{R}_0$ and process noise covariance $\mathbf{Q}_0$ are used for state estimation. If the time step k surpasses L_0, the ICM $\mathbf{H}_k$ will be updated with the selected EIS based on the adaptive window length following Eq. (39). As shown in the yellow part of Fig. 2. Following the estimation of ICM $\mathbf{H}_k$, the covariance of the measurement noise ($\mathbf{R}_k$) and process noise ($\mathbf{Q}_k$) are updated. The number N_t in Fig. 2 represents the total length of the time sequence in the random charge and discharge test.

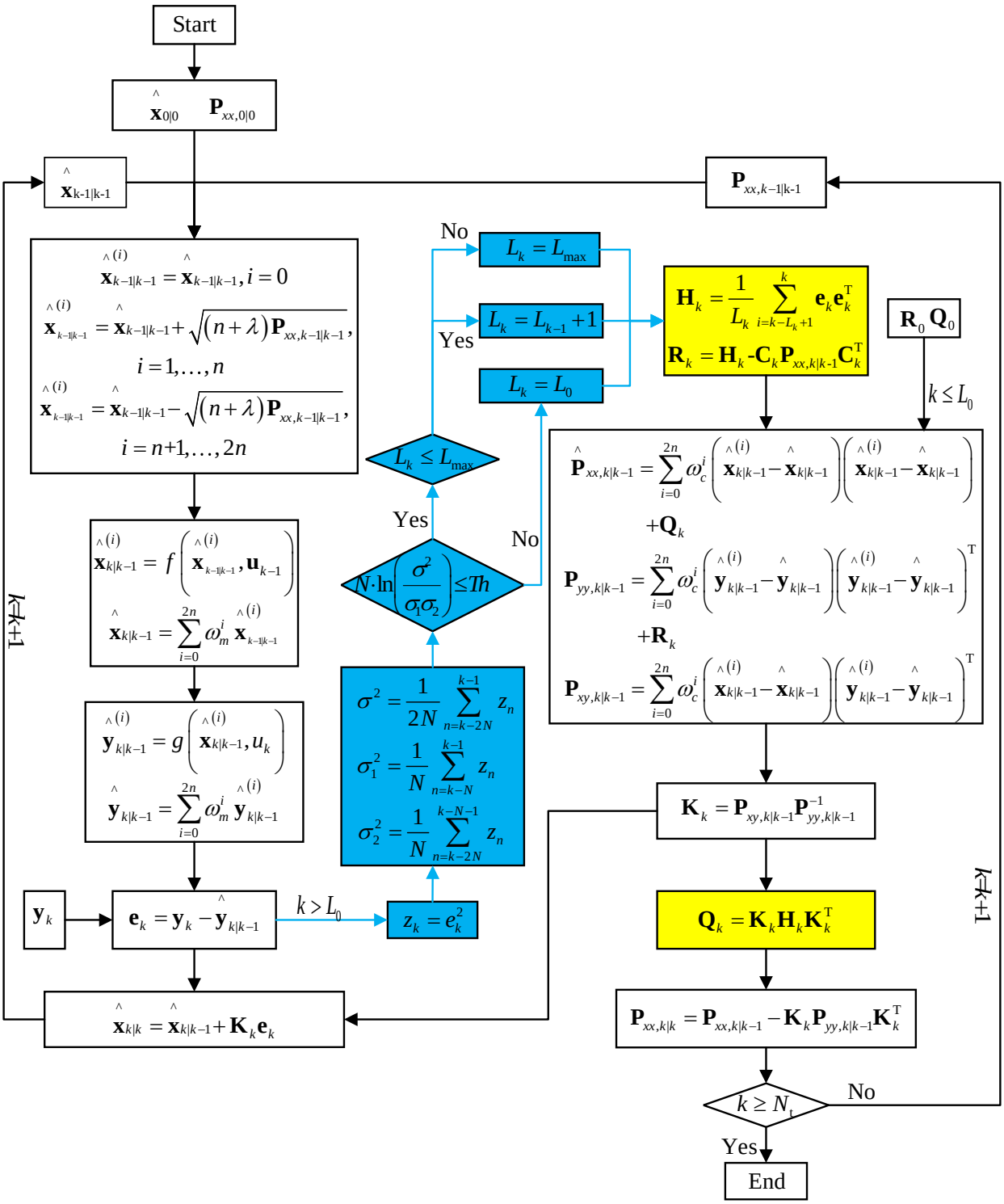

Fig. 2. Flow chart of IAUKF-based SOC estimation

4 Results and discussion

4.1 Parameter identification of the ECM

The random charge and discharge test data (RW9.mat) provided by NASA PCoE [49] is used to verify the proposed IAUKF method. The test object is the 2nd generation 18650 LiCoO2 battery provided by Idaho National Laboratory. The nominal capacity of the battery is 2.1002Ah. The battery is tested at 25 ℃. The load current is randomly generated every five minutes. The current ranges from -4.5A to 4.5A. The negative current represents the charge of the battery, and the positive current represents the discharge of the battery. Here, the polynomial function is chosen to model the OCV data. The degree of polynomial function is the key parameter that affects the modelling accuracy of OCV. If the selected degree of polynomial function is low, the OCV model is under-fitting. If the selected degree of polynomial function is large, the OCV model will be over-fitting. By trial, the 12-degree polynomial function is selected to model the OCV data. Based on the polynomial fitting, the parameters $(K_0, K_1, \ldots, K_n)$ of the OCV model are obtained. Fig. 3 shows the original data and fitting results, and Table 1 lists the corresponding parameters. The RMSE and MAE of the OCV estimation are 0.00337 V and 0.00264V, respectively, indicating that the proposed 12-degree polynomial OCV model has high accuracy.

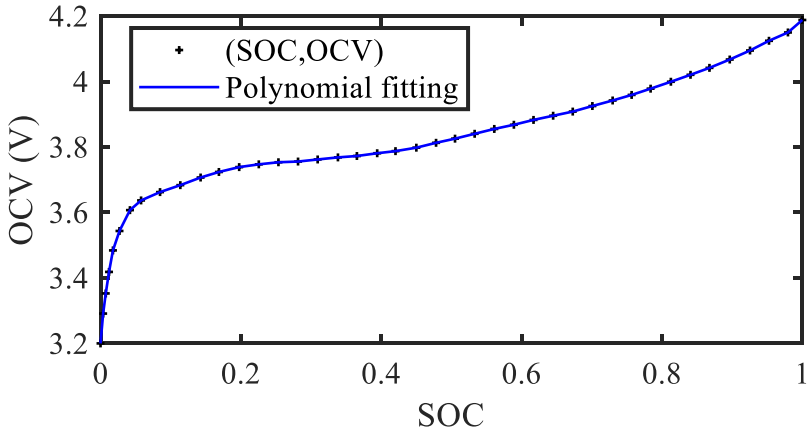

Fig. 3. OCV-SOC measurement points and polynomial fitting curve

Table 1. Parameters of OCV model

K_i	K_0	K_1	K_2	K_3	K_4	K_5
value	-3.884e+4	2.503e+5	-7.131e+5	1.183e+6	-1.266e-6	9.151e+5

K_6	K_7	K_8	K_9	K_{10}	K_{11}	K_{12}
-4.537e+5	1.540e+5	-3.497e+4	5.093e+3	-444.544	21.481	3.212

With the obtained OCV model, the initial parameters of the ECM can be estimated based on GA in the MATLAB R2018b Optimization Toolbox with default parameters. The pulse discharge current and the corresponding terminal voltage are shown in Fig. 4, from which the initial parameters (R_s, R_p, C_p) of the ECM can be estimated. The results are shown in Table 2.

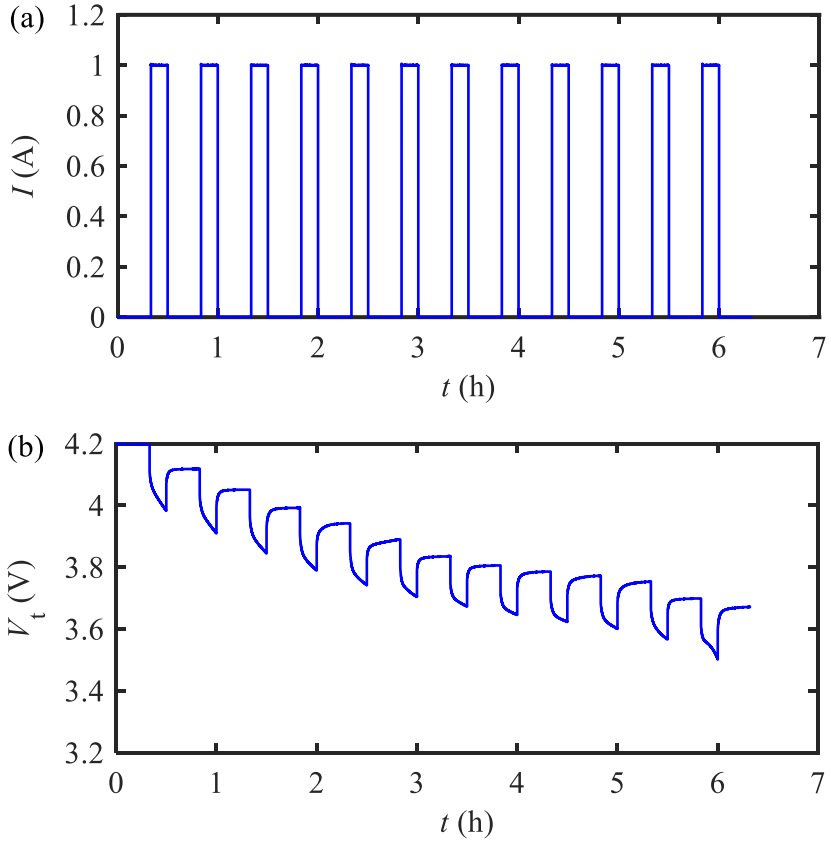

Fig. 4. (a) Pulse discharge current, and (b) terminal voltage

Table 2. Initial parameter values of 1RC model

Parameter	R_s	R_p	C_p
value	0.074	0.045	815

The test data can be downloaded from the official website of NASA. The URL of this website is attached in the **Acknowledgement**. The test data covers a significant time (6.76 hours) due to the relatively lengthy charge step. So, the terminal voltage and current within the 1st hour of the test data are used to verify the proposed IAUKF method. Fig. 5 shows the terminal voltage and current of the battery during the random charge and discharge test.

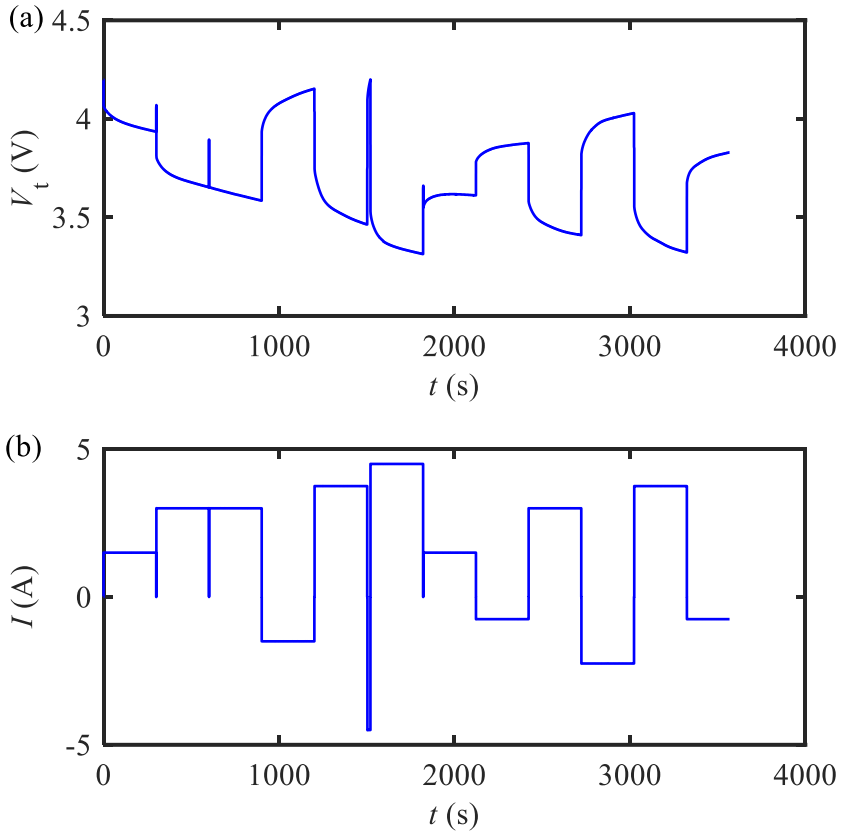

Fig. 5. (a) Battery terminal voltage V_t, and (b) current I under random discharge and charge test

With the obtained initial parameter values, FF-RLS is used to estimate these parameters online. Typically, the forgetting factor in the FF-RLS is set to a value between 0.95 and 1. In this paper, the forgetting factor in the FF-RLS is set to 0.99. The estimated parameter results are shown in Fig. 6. The characteristic of parameter change is closely related to the random discharge and charge current and SOC, as shown in Fig. 5. The battery is charged or discharged every five minutes with the randomly generated current. This process is stopped for a very short time (about 1 second) before the

next random current pulse. During the short rest period, the sampling time of the current/voltage signals changes from 1s to 0.04s. Therefore, the parameter update scheme was stopped during the short rest period and the ECM parameters are kept the same as the last estimated value before the short rest period. Fig. 6 shows the parameter identification results of the ECM.

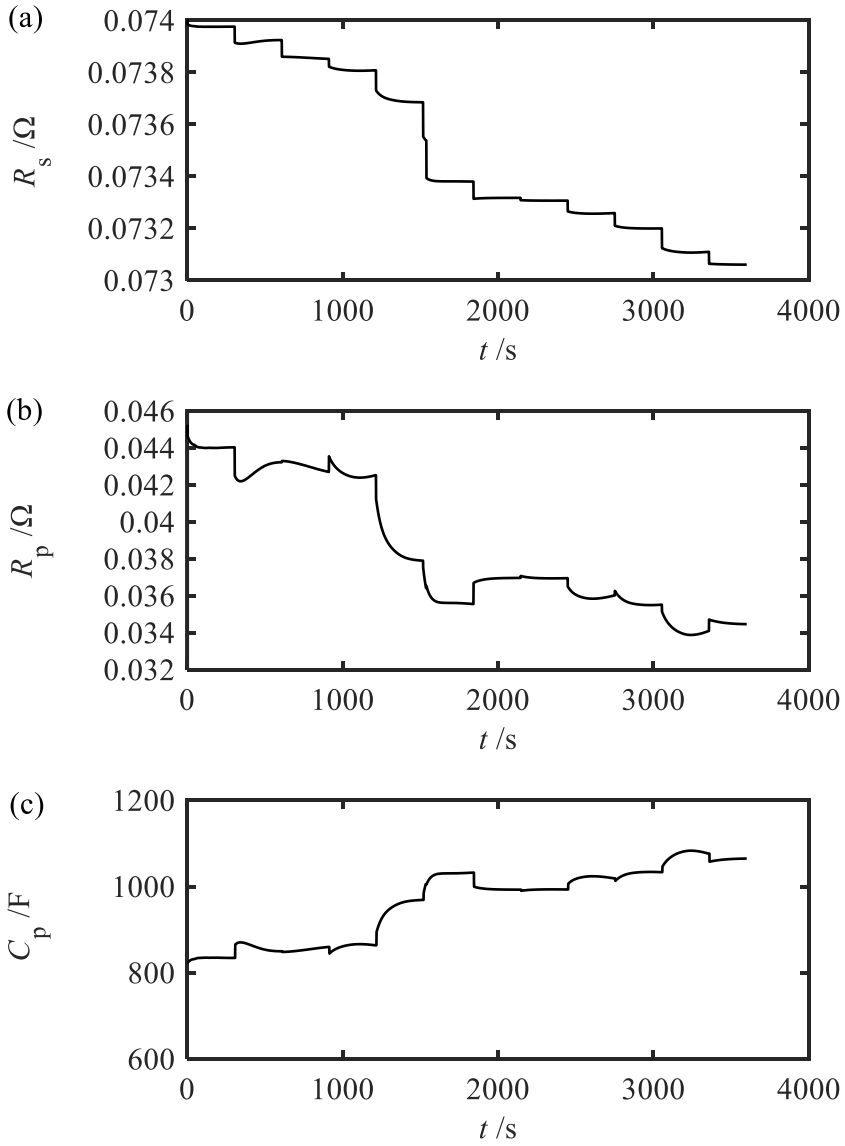

Fig. 6. Estimated parameter values of R_s, R_p and C_p

The estimated terminal voltage and its error are shown in Fig. 7. The estimated terminal voltage in blue matches very well with the measured one in black, as shown in Fig. 7(a). The error of the terminal voltage is kept low, as shown in Fig. 7(b), except for a few small error spikes that occur at the beginning of these short stop periods. The reason is that the sampling time changes during these

short stop periods. If the sampling time interval Δt changes, which means $\exp\left(-\frac{\Delta t}{R_p C_p}\right)$ in the FF-RLS algorithm [47] changes, model parameters should change. The parameter update scheme was stopped during the short stop periods and the ECM parameters are kept the same as the last estimated values before the short stop periods. The RMSE and MAE of terminal voltage are 0.00108 and 0.00063, respectively, which indicates the high accuracy of the parameter identification of the ECM. The error of terminal voltage changes during the charge and discharge process, which depends on the load current dynamics and error of battery model. These factors will lead to the distribution change of the EIS in the AUKF-based SOC estimation.

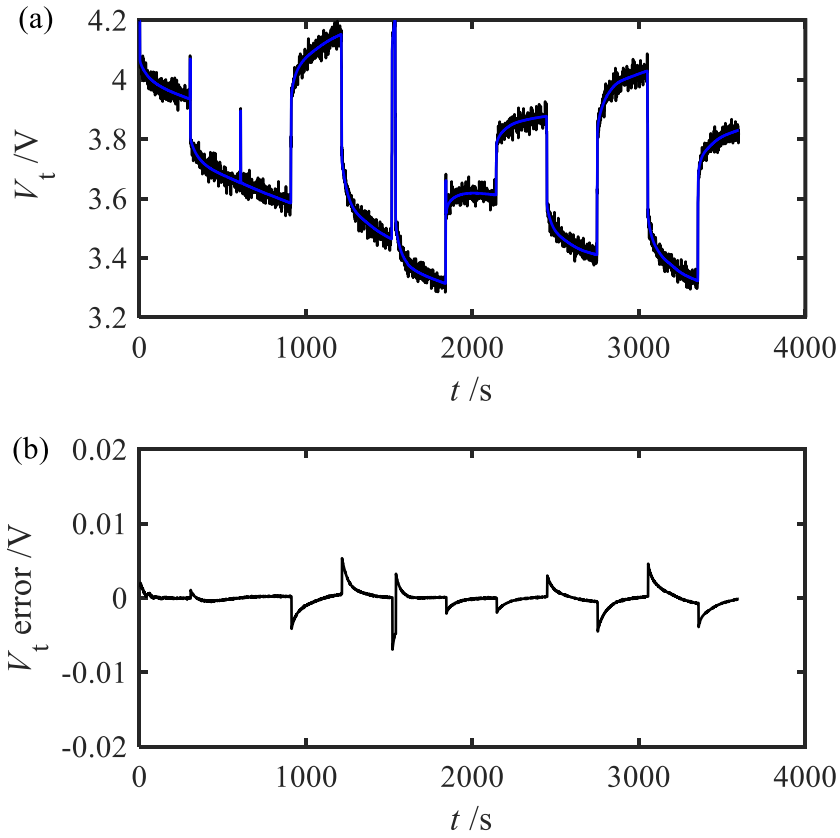

Fig. 7. (a) Estimated terminal voltage, and (b) its error using the FF-RLS method for online parameter estimation

4.2 Verification of IAUKF-based SOC estimation

4.2.1 Verification of IAUKF method under random walk discharge condition

The initial parameters [50] required for IAUKF-based SOC estimation are listed in Table 3.

Table 3. Initial parameter values for SOC estimation

Parameters	value
Initial state $\mathbf{x}_0=[V_p, \mathrm{SOC}]$	$[0\ 0.95]^T$
Initial state error covariance matrix $\mathbf{P}_0$	[1e-3, 0; 0, 3e-4]
Process noise covariance matrix $\mathbf{Q}_0$	[1e-4, 0; 0, 5e-4]
Measurement noise covariance matrix $\mathbf{R}_0$	5e-3

Fig. 8 shows the calculated EIS during the process of the SOC estimation of the battery. Based on the theoretical analysis above, the EIS can be affected by both load current dynamics and the error of the battery model. As shown in Fig. 8, it is obvious that the EIS does not follow the Gaussian distribution with zero mean value and fixed variance during the whole charge and discharge process. Therefore, the ICM should not be estimated with fixed length EIS. The border of the distribution change of the EIS should be detected, and the ICM should be updated with the EIS after that border.

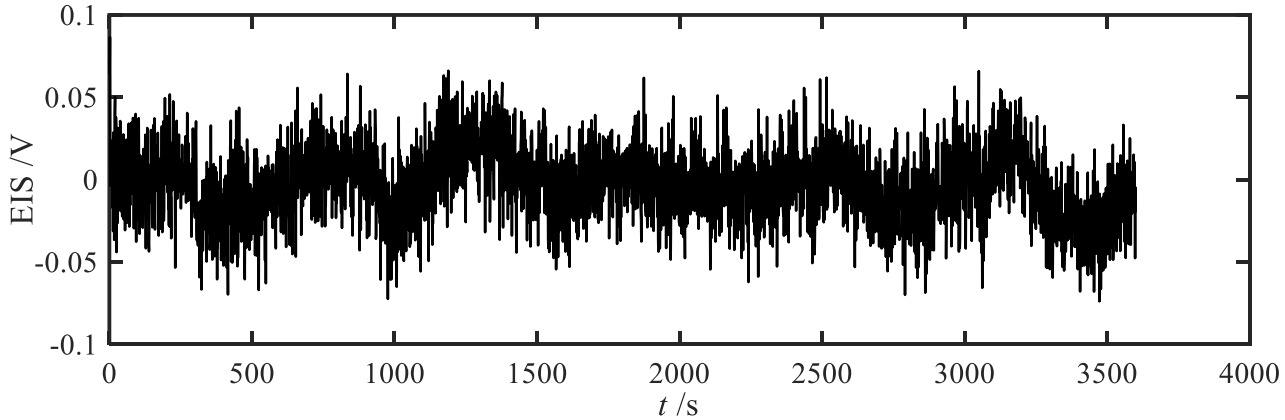

Fig. 8. Error innovation sequence

Based on the IAUKF method, the border of the distribution change of the EIS is detected. Then the window length of EIS is updated according to adaptive rule described by Eq. (39). The maximum length $L_{\max}$ of the sliding detection window is set to 8, and the threshold Th=4.0 by trial method. The initial length of the sliding detection window is set to 2.

The window length of the selected EIS gradually increases if $ML_2 - ML_1$ is less than the specified threshold, which means that the distribution of the EIS does not change significantly. On the other hand, if $ML_2 - ML_1$ exceeds the specified threshold and a EIS distribution change is detected, the window length of the selected EIS will be reset to 2 in order to update the ICM. In order to show the length of the selected EIS clearly, the total time window [0, 3600] are separated into three parts, as shown in Fig. 9 (a), (b) and (c). The results show that the window length of the selected EIS constantly cycles from 2 to 8, indicating successful detections of the locations of the EIS distribution changes. In order to illustrate the adaptive rule clearly, the local enlarged drawing ranging from 1450 to 1550 is shown in Fig. 9 (d).

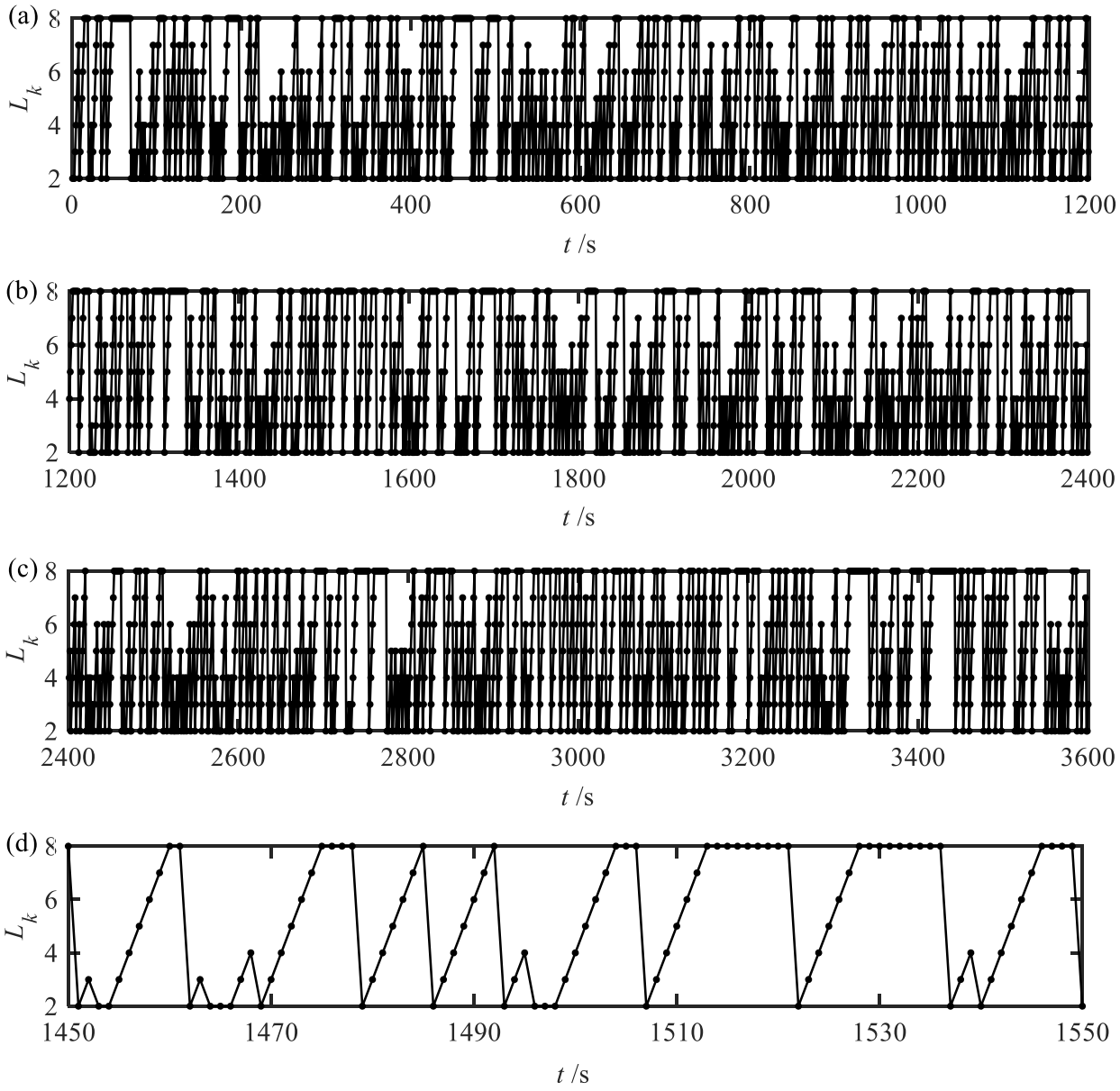

Fig. 9. (a), (b) and (c) Selected EIS length, and (d) local enlarged drawing

The selected EIS will be used to estimate the ICM, according to Eq. (43). Then the covariance of measurement and process noise are estimated based on Eq. (24) and (25) with the obtained ICM. Based on the proposed IAUKF method, the SOC estimation results are shown in Fig. 10. It shows that the SOC estimation results based on the IAUKF are very close to the reference SOC. The local enlarged drawing in Fig. 10 (a) shows that the SOC converges quickly to the reference SOC. Fig. 10 (b) shows that the SOC error quickly converges to zero. The approximately constant error, as shown

in Fig. 10(b), is caused by the measurement error and model error. In order to demonstrate the superiority of the IAUKF method, the SOC results based on AEKF and AUKF methods are given as a comparison, as shown in Fig. 10. For AEKF method, the initial parameter values are the same as those values listed in Table 3. But the best window length for AEKF is 4 under random walk discharge condition. Although the AUKF method can quickly converge to near the reference SOC. However, the SOC error constantly fluctuates above the reference SOC, as shown in Fig. 10(b). The AUKF parameters are initialized with the same values listed in Table 3. The fixed window length of the EIS in the AUKF method is 8. The local enlarged drawings in Fig. 10 (a) shows that the SOC result based on IAUKF is closer to the reference SOC than the one based on AUKF method. As shown in Fig. 10 (b), the SOC error based on IAUKF method is significantly lower than that based on the AUKF method, which shows the better performance of the proposed IAUKF method.

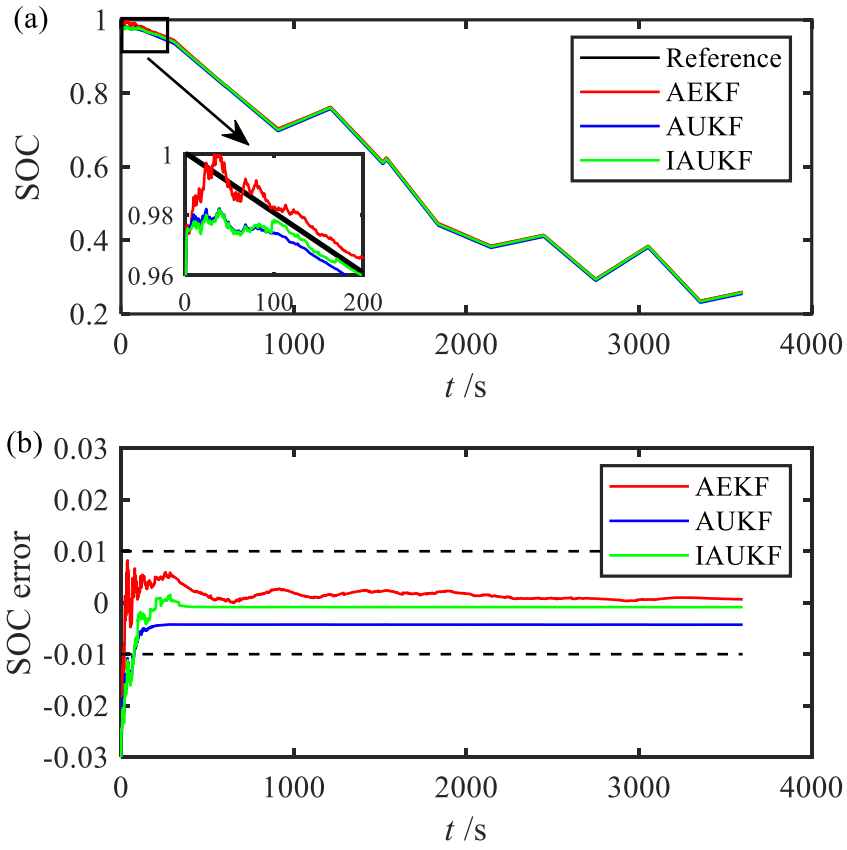

Fig. 10. (a) Estimated SOC, and (b) its error under different methods

The reason is that the estimated ICM in the IAUKF method is different from the one in the AUKF method, as shown in the local enlarged drawing in Fig. 11. Since the covariance of measurement and process noise are updated based on the ICM according to Eq. (24) and (25), the relative magnitude between measurement and process noise covariance will change. From Fig. 11, it can be concluded that the IAUKF method can update the covariance faster than the AUKF method, leading to improvement of the SOC accuracy. This is because the IAUKF can detect the point of the EIS distribution change.

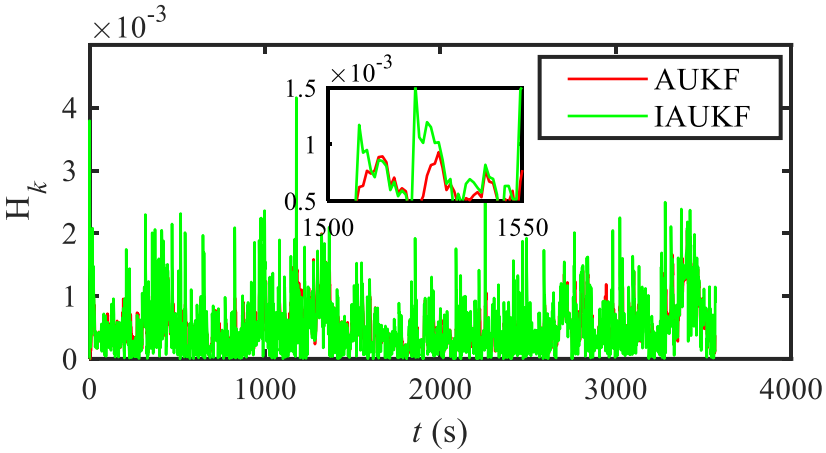

Fig. 11. ICM $\mathbf{H}_k$ under different methods

To quantitatively compare the performance of these two methods, the corresponding RMSE and MAE of SOC estimation results are listed in Table 4. Compared with the AUKF method, the RMSE and MAE of the proposed IAUKF decrease by 43.70% and 72.37% respectively, which demonstrates the superiority of the proposed method.

Table 4. RMSE and MAE of SOC under different methods

Method	AEKF	AUKF	IAUKF
RMSE	0.00239	0.00492	0.00277
MAE	0.00165	0.00456	0.00126

For online SOC estimation of lithium-ion battery, the computation time is another key index that must be evaluated. The computation time of the proposed IAUKF method is compared with the one of the AUKF method. This computational time is the execution time of MATLAB script on a PC with Intel Core(TM) i7-4710MQ processor and 8.0GB memory. The computation time for the same

method may be slightly different when it is executed at different time even with the same PC. The reason is that the computation time is affected by the current state of system, such as CPU, memory and so on. In order to accurately evaluate the computation time of the proposed IAUKF method, the MATLAB script of the proposed IAUKF method is executed for 10 times to obtain the statistics of computation time.

The statistics of computation time of different methods is listed in Table 5. The computation time of AEKF method takes the minimum value among three methods. Compared with the AUKF method, the average computation time of the proposed IAUKF method only slightly increases by 6.27%. The standard error of the computation time of the two methods are at the same level. The increased computation time of the proposed IAUKF method is mainly contributed by the additional detection algorithm for EIS distribution change. However, the proposed IAUKF method has a shorter average window length for ICM estimation which helps reduce the computation time. In the AUKF method, the EIS window length used for ICM estimation is constant 8. However, in the proposed IAUKF method, the EIS window length changes from 2 to 8, as shown in Fig.9. Thus, the average window length of the EIS used for the ICM estimation of the proposed IAUKF method is shorter than the one of the AUKF method. In summary, the proposed IAUKF method can significantly improve the SOC estimation accuracy by slightly sacrificing the computation time.

Table 5. Computation time under different methods

Method	AEKF	AUKF	IAUKF
Average computation time (s)	0.879	1.8027	1.916
Standard error of computation time (s)	0.0209	0.0391	0.0402

4.2.2 Verification of IAUKF method under DST and FUDS conditions

In order to verify the effectiveness of the IAUKF method for other discharge conditions, discharge test data of LIBs under DST and FUDS conditions are used to evaluate the performance of SOC estimation. These discharge test data are provided by Center for Advanced Life Cycle Engineering (CALCE) of Maryland University [9]. The test object is INR 18650-20R. The cell

chemistry is LNMC/Graphite. The rated capacity of the test object is 2Ah. The discharge test of LIBs is implemented under 25℃. Considering that the SOC error fluctuation mainly occurs in the initial convergence phase, the first 1h test data are used for verifying the proposed IAUKF method.

Based on the incremental test method, the SOC-OCV data for INR 18650-20R can be obtained. In order to obtain accurate OCV model, ten-degree polynomial is used to build the OCV model for INR 18650-20R. The coefficients of polynomial OCV model for INR 18650-20R is listed in Table. 6.

Table 6. Parameters of OCV model of INR 18650-20R

$K_i^{'}$	$K_0^{'}$	$K_1^{'}$	$K_2^{'}$	$K_3^{'}$	$K_4^{'}$	$K_5^{'}$
value	8.772e+3	-4.370e+4	9.313e+4	-1.110e+5	8.100e+4	-3.735e+4

$K_6^{'}$	$K_7^{'}$	$K_8^{'}$	$K_9^{'}$	$K_{10}^{'}$
1.080e+4	-1.862e+3	1.667e+2	-4.001	3.298

The parameters ($R_s^{'}$, $R_p^{'}$ and $C_p^{'}$) of ECM of INR 18650-20R can be obtained based on GA algorithm, as listed in Table 7. The RMSE and MAE of the ECM of INR 18650-20R is 5.988e-4 and 3.708e-4 respectively, which demonstrates that 1RC ECM can accurately model the dynamic behaviour of INR 18650-20R under 25℃.

Table 7. Initial parameter values of 1RC model of INR 18650-20R

Parameter	$R_s^{'}$	$R_p^{'}$	$C_p^{'}$
value	0.0710	0.0342	1135.2

For DST condition, the initial parameter values for SOC estimation based on IAUKF method are listed in Table 8.

Table 8. Initial parameter values for SOC estimation of INR 18650-20R (DST)

Parameters	value
Initial state $\mathbf{x}_0^{'}=[V_p, \mathrm{SOC}]$	$[0\ 0.5]^T$
Initial state error covariance matrix $\mathbf{P}_0^{'}$	[1e-4, 0; 0, 2e-2]
Process noise covariance matrix $\mathbf{Q}_0^{'}$	[1e-3, 0; 0, 6.5e-3]
Measurement noise covariance matrix $\mathbf{R}_0^{'}$	5e-3

The initial real SOC of INR 18650-20R is 0.8. For IAUKF method, the initial window length is set to 60. The maximum window length is set to 120. The threshold Th is set to 100. For AUKF method, the window length for AUKF method is set to 120. Other initial parameter values in AUKF

method are the same as that in IAUKF method. For AEKF method, the initial parameter values are the same as those listed in Table 8. But the best window length for AEKF is 10 under DST condition. The SOC estimation results of AEKF, AUKF and IAUKF methods are shown in Fig. 12. Fig.12 shows that the SOC estimation performance of IAUKF method is the best among three methods under DST condition. The convergence performance of AEKF method is better than that of AUKF method. Fig. 12 shows that the SOC estimation result based on IAUKF method can quickly convergence to the reference SOC. However, the SOC estimation result based on AUKF method can't converge to the reference SOC.

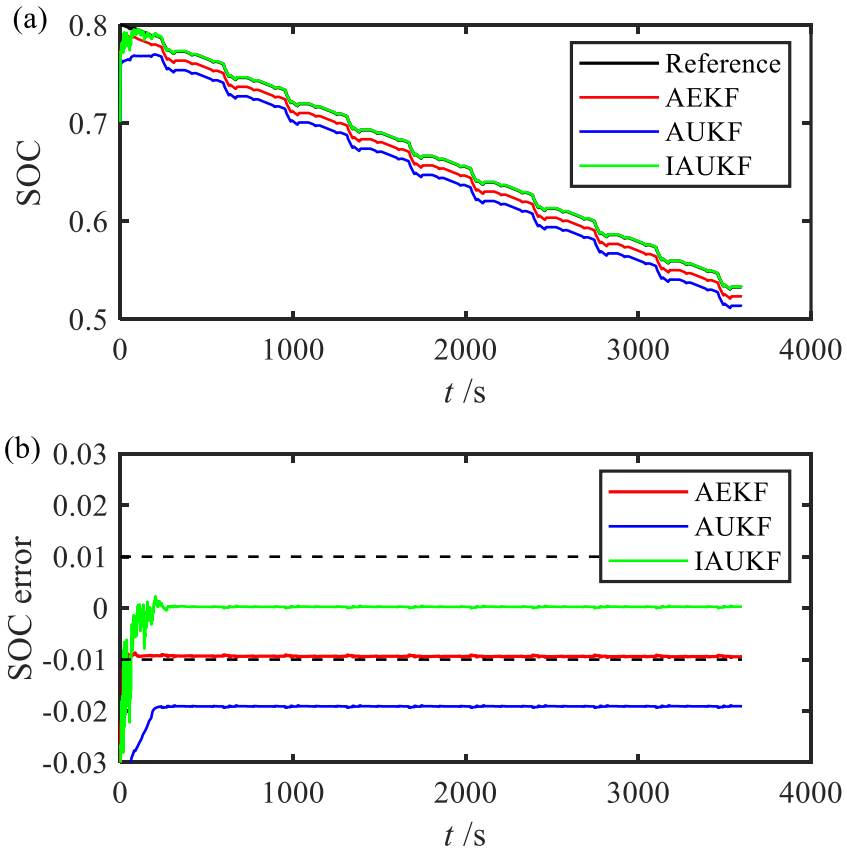

Fig. 12. (a) Estimated SOC, and (b) its error under different methods (DST)

To quantitatively compare the performance of these two methods, the corresponding RMSE and MAE of SOC estimation results are listed in Table 9. Both RMSE and MAE of SOC based on IAUKF method take the minimum values among these three methods. Compared with the AUKF

method, the RMSE and MAE of the proposed IAUKF decrease by 85.05% and 96.94% respectively, which demonstrates the superiority of the proposed method.

Table 9. RMSE and MAE of SOC under different methods (DST)

Method	AEKF	AUKF	IAUKF
RMSE	0.00942	0.0198	0.00296
MAE	0.00946	0.0196	0.00066

The computation time for different methods are listed in Table 10. The computation time of AEKF method takes the minimum value among three methods. The computation time of IAUKF method slightly increases by 4.90% compared with that of AUKF method. The reason is that the increased time is mainly caused by the detection algorithm for EIS distribution change.

Table 10. Computation time under different methods (DST)

Method	AEKF	AUKF	IAUKF
Average computation time (s)	0.594	0.971	1.021
Standard error of computation time (s)	0.0247	0.065	0.093

For FUDS condition, the initial parameter values for SOC estimation based on IAUKF method are listed in Table 11.

Table 11. Initial parameter values for SOC estimation of INR 18650-20R (FUDS)

Parameters	value
Initial state $\mathbf{x}_0^{"}=[V_p, \mathrm{SOC}]$	$[0\ 0.5]^T$
Initial state error covariance matrix $\mathbf{P}_0^{"}$	[1e-6, 0; 0, 6e-3]
Process noise covariance matrix $\mathbf{Q}_0^{"}$	[1e-4, 0; 0, 1e-3]
Measurement noise covariance matrix $\mathbf{R}_0^{"}$	5e-3

The initial SOC of INR 18650-20R is 0.8. For IAUKF method, the initial window length is set to 160. The maximum window length is set to 400. The threshold Th is set to 300. For AUKF method, the window length for AUKF method is set to 400. Other initial parameter values in AUKF method are the same as that in IAUKF method. For AEKF method, the initial parameter values are the same as those listed in Table 11. But the best window length for AEKF is 10 under FUDS condition. The SOC estimation results of AEKF, AUKF and IAUKF methods are shown in Fig. 13. Fig. 13 shows that the SOC estimation result based on IAUKF method can gradually converge to the reference SOC. The performance of IAUKF method is the best performance among these three methods. The SOC

estimation result based on AUKF and AEKF methods can't converge to the reference SOC. The local enlarged drawing in Fig. 13(a) shows that the SOC estimation curves of AUKF and IAUKF method separate after about 200s. Then, the SOC estimation curve of IAUKF method gradually converges to the reference SOC. The reason is due to the intelligent noise estimator which can detect the distribution change of EIS.

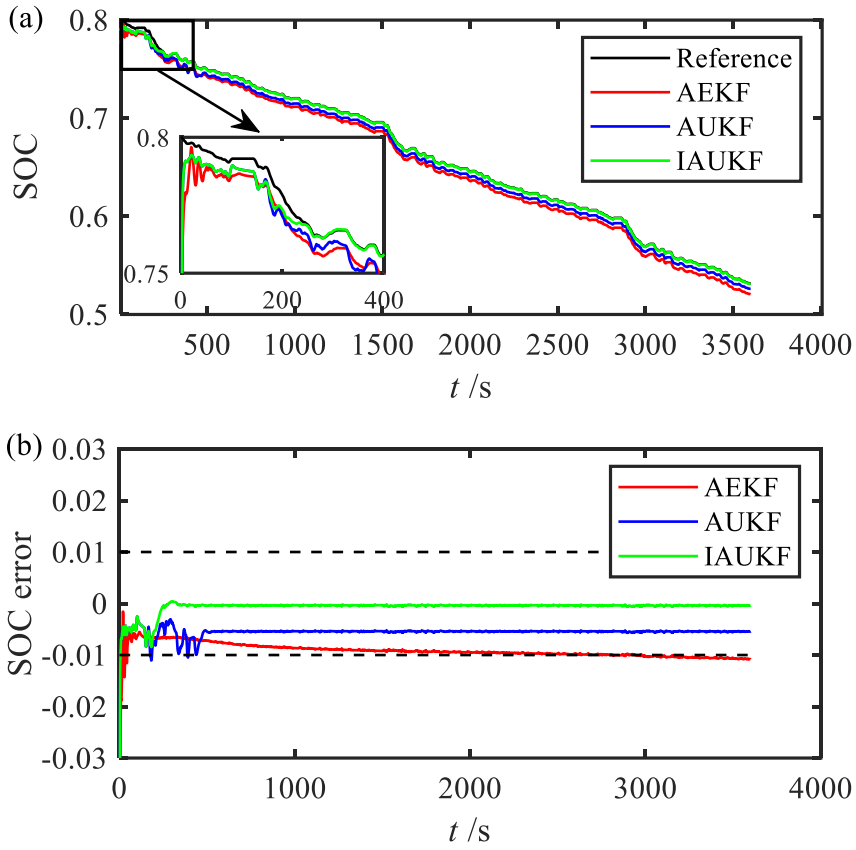

Fig. 13. (a) Estimated SOC, and (b) its error under different methods (FUDS)

To quantitatively compare the performance of these two methods, the corresponding RMSE and MAE of SOC estimation results are listed in Table 12. Table 12 indicates that the proposed IAUKF method achieves the best performance for SOC estimation among these three methods. Compared with the AUKF method, the RMSE and MAE of the proposed IAUKF decrease by 44.53% and 86.12% respectively, which demonstrates the superiority of the proposed method.

Table 12. RMSE and MAE of SOC under different methods (FUDS)

Method	AEKF	AUKF	IAUKF

RMSE	0.00919	0.00649	0.00360
MAE	0.00970	0.00560	0.00078

The computation time for different methods are listed in Table 13. The computation time of AEKF method takes the minimum value among three methods. The computation time of IAUKF method slightly increases by 7.73% compared that of AUKF method. The reason is that the detection algorithm for EIS distribution change lead to the increase of computation time.

Table 13. Computation time under different methods (FUDS)

Method	AEKF	AUKF	IAUKF
Average computation time (s)	0.602	0.957	1.031
Standard error of computation time (s)	0.0251	0.0286	0.0424

To sum up, the proposed IAUKF method can significantly improve the SOC estimation performance of LIBs at the cost of slightly increase of computation time.

4.3 Effect analysis of key parameters on SOC estimation

In Section 4.3, effect analysis of key parameters is the key point. The method of effect analysis of key parameters on SOC estimation under different discharge condition is similar. In order to avoid a lengthy article, in Section 4.3, we still choose the random discharge condition to analyse the effect of key parameters on SOC estimation.

4.3.1 Effect of the initial window length of EIS on the SOC estimation

The SOC accuracy is affected by the relative magnitude of the measurement and process noise covariances. According to Eq. (24) and (25), the covariance of measurement and process noise are updated based on the ICM, which is estimated by the selected EIS. Therefore, the initial window length of the EIS will affect SOC estimation accuracy. The effect of the initial window length of the EIS on SOC estimation is evaluated, as shown in Fig. 14.

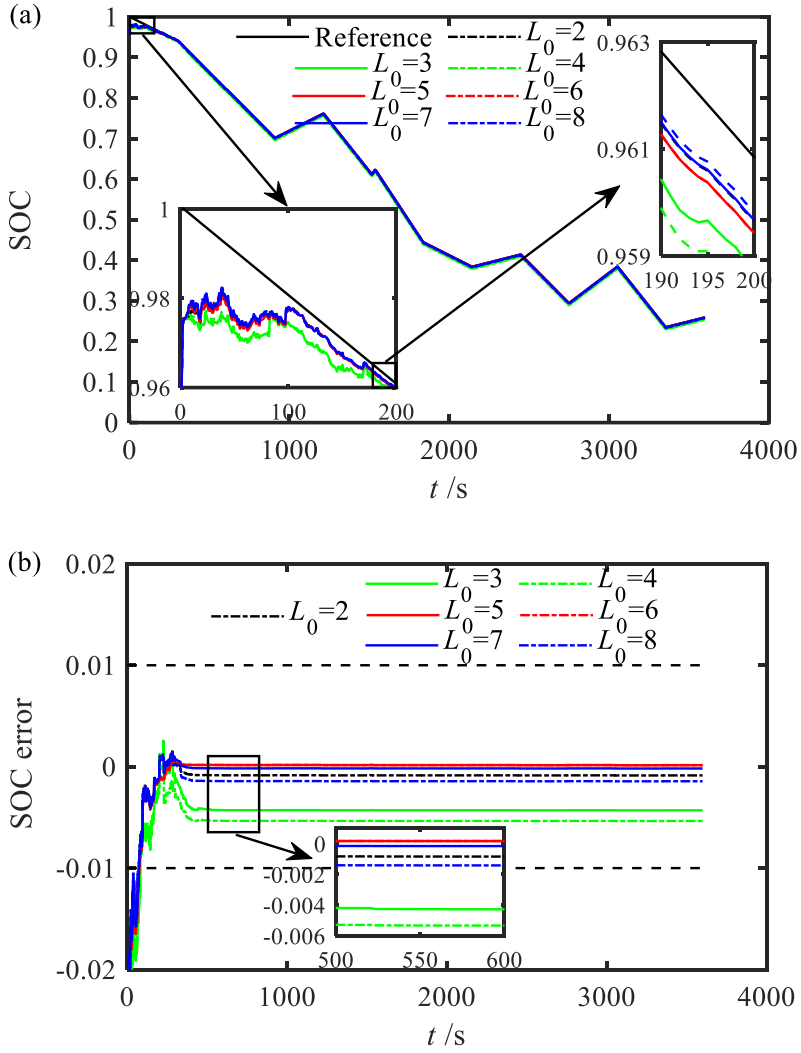

Fig. 14. Effect of L_0 of the EIS on (a) SOC and (b) its error based on IAUKF method

As shown in Fig. 14(a), the SOC converges to the reference SOC quickly in less than 100 seconds. The SOC accuracy can be classified into two groups according to the size of SOC error, as shown in Fig. 14(b). The SOC error based on the proposed IAUKF is very close to each other when initial window length is set to 2, 5, 6, 7 and 8, which are categorized as the first group. The SOC error based on the proposed IAUKF is very close to each other when initial window length is set to 3 and 4, i.e., the second group. The reason is that the initial window length has an effect on the ICM $\mathbf{H}_k$. The estimated ICM $\mathbf{H}_k$ under different initial window length is shown in Fig. 15(a). The local enlarged drawing is shown in Fig. 15(b). Fig. 15(b) shows that the ICM $\mathbf{H}_k$ can also be classified into two

groups according to the classification mentioned above. The ICM $\mathbf{H}_k$ will affect the update of covariance of measurement and process noise, and leads to two groups of SOC accuracy with significant difference. Therefore, a proper L_0 should be selected by trial and error.

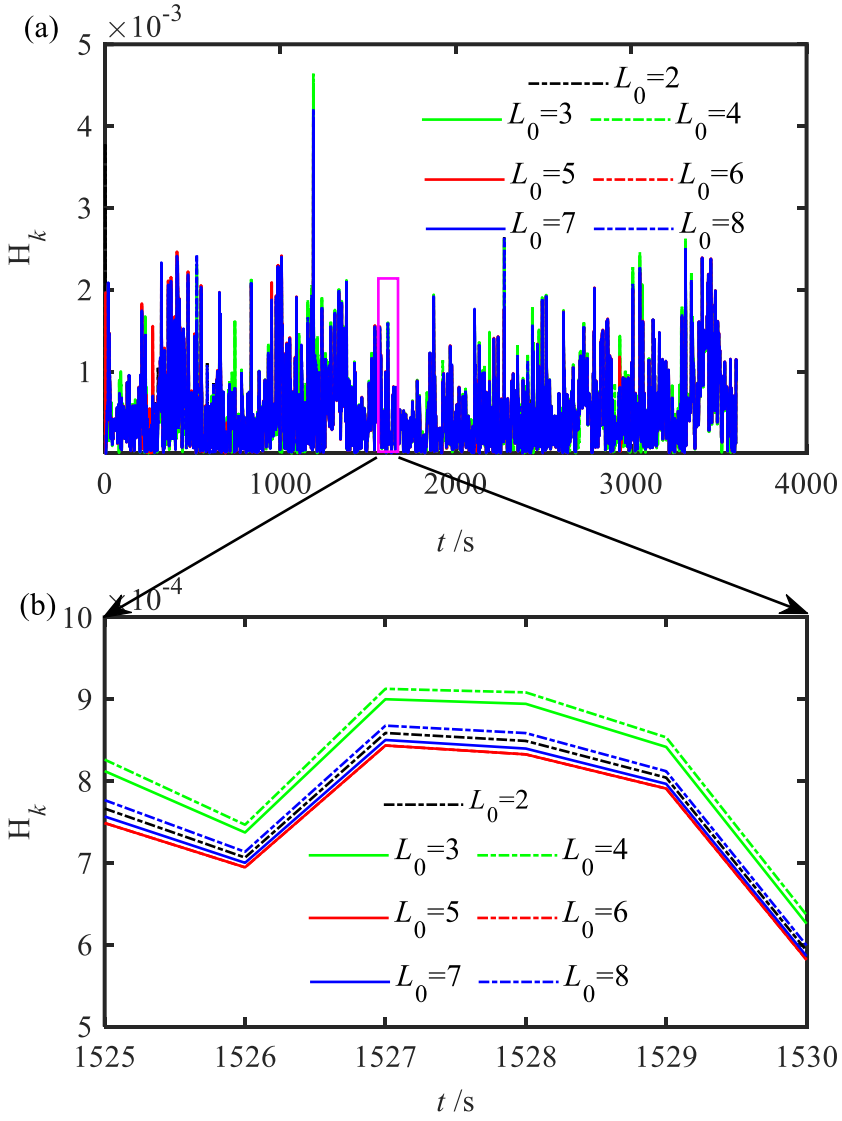

Fig. 15. Effect of L_0 on (a) ICM $\mathbf{H}_k$, and (b) local enlarged drawing based on IAUKF method

To quantitatively evaluate the effect of the initial window length of the EIS on the SOC estimated based on the IAUKF, the corresponding RMSE and MAE of SOC are listed in Table 14. The SOC accuracy based on the proposed IAUKF is very close to each other when initial window length is set to 2, 5, 6, 7 and 8, which are categorized as the first group. The SOC accuracy based on

the proposed IAUKF is very close to each other when initial window length is set to 3 and 4, i.e., the second group. The SOC accuracy of the second group is lower than the one of the first group. Therefore, selecting proper initial window length can further improve the SOC accuracy based on the proposed IAUKF method. Therefore, the initial window length should be tuned properly by trial and error.

Table 14. RMSE and MAE under different initial length of EIS

IAUKF	L_0=2	L_0 = 3	L_0=4	L_0=5	L_0=6	L_0=7	L_0=8
RMSE of SOC	0.00277	0.00515	0.00596	0.00266	0.00266	0.00255	0.00284
MAE of SOC	0.00126	0.00453	0.00553	0.00064	0.00063	0.00064	0.00176

4.3.2 Effect of the threshold value on the SOC estimation

The threshold Th is also an important parameter that affects the SOC accuracy based on the proposed IAUKF method. The effect of the threshold Th on the SOC estimation is also analysed, as shown in Fig. 16. Fig. 16(a) indicates that the SOC converges to the reference SOC quickly with time. As shown in Fig. 16(b), the SOC errors described by red and blue dot lines ($Th = 4.3$, and $Th = 4.5$, respectively) are almost overlapped, and are very close to zero. The SOC errors described by red and blue dot lines ($Th = 4.3$, and $Th = 4.5$, respectively) are significantly lower than those in the remaining parts. By calculating the window length of the EIS, it can be found that L_k is similar when Th is set to 4.3 and 4.5, as shown in Fig. 17(a), (b) and (c). As shown in the local enlarged drawing in Fig. 17(d), L_k is almost equal when Th is set to 4.3 and 4.5. Similar window length of the EIS will lead to similar ICM. The similar ICM will lead to similar relative magnitude between covariance of measure and process noise, which affects the SOC accuracy directly. Due to the same reason, the SOC errors described by green dot line and red solid line ($Th = 4.1$, and $Th = 4.2$, respectively) are almost completely overlapped, as shown in the local enlarged drawing in Fig. 16(b).

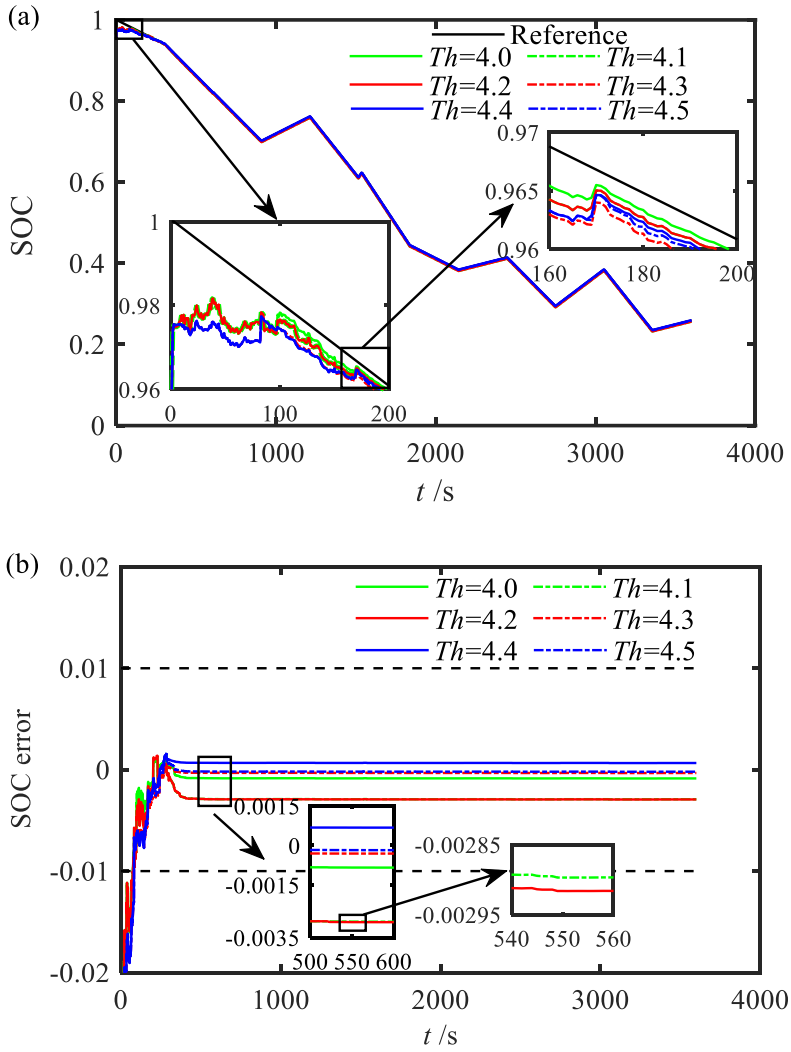

Fig. 16. The effect of Th on (a) SOC and (b) its error based on IAUKF method

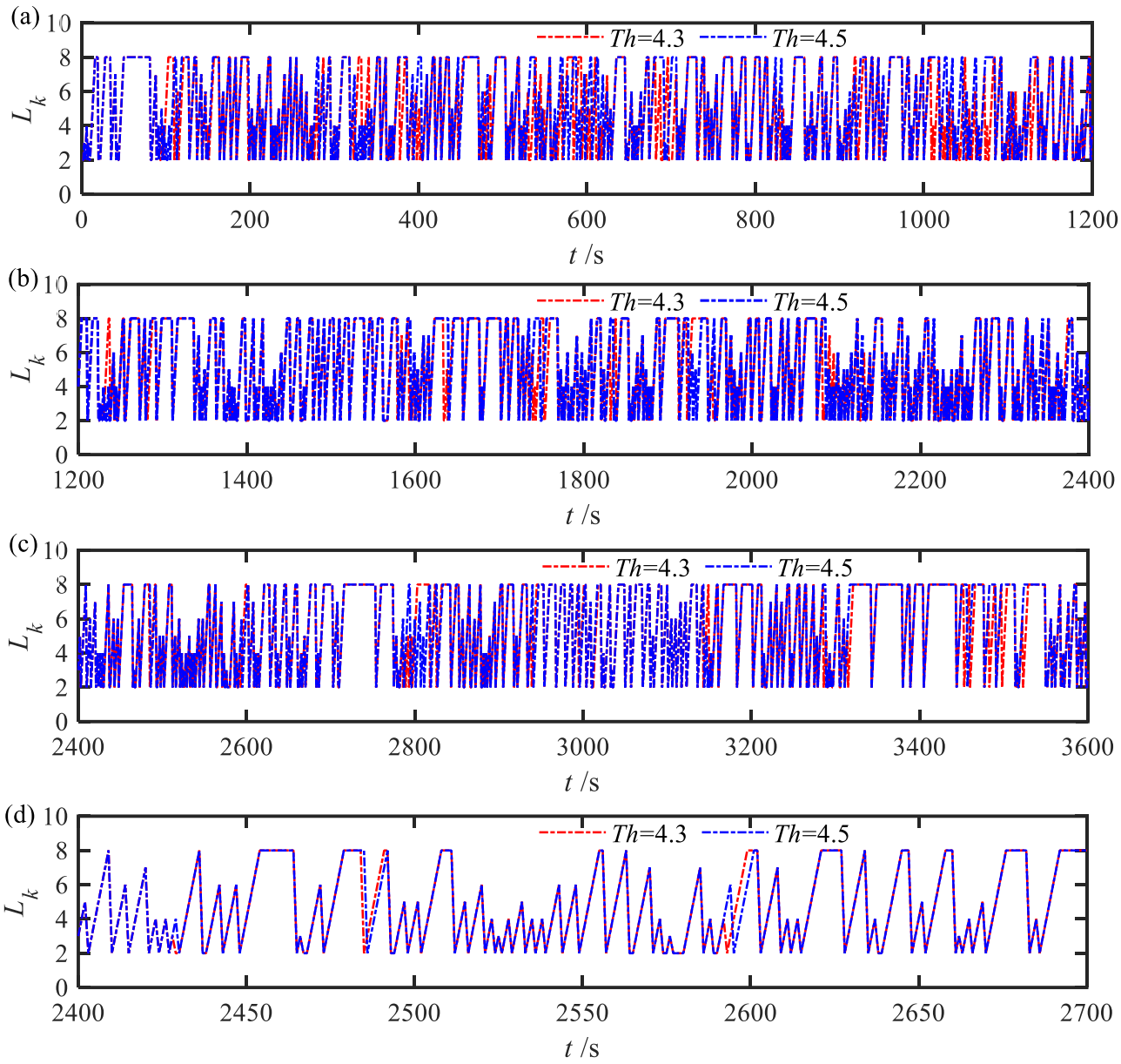

Fig. 17. (a), (b) and (c) Window length of EIS and (d) its local enlarged drawing

In order to quantitatively evaluate the effect of the threshold Th on the SOC estimation based on the proposed IAUKF, the corresponding RMSE and MAE of SOC are listed in Table 15. It can be found that the RMSE and MAE of SOC are close to each other when the threshold Th is set to 4.3 and 4.5. The MAE of SOC when the threshold Th is set to 4.3 and 4.5 is significantly lower than the one of the remaining parts. Therefore, the threshold Th should be tuned properly by trial and error method to further improve the SOC accuracy.

Table 15. RMSE and MAE under different thresholds

IAUKF	*Th*=4.0	*Th*=4.1	*Th* = 4.2	*Th*=4.3	*Th*=4.4	*Th*=4.5
RMSE of SOC	0.00277	0.00387	0.00388	0.00317	0.00322	0.00316
MAE of SOC	0.00126	0.00317	0.00319	0.00095	0.00126	0.00083

4.3.3 Effect of the initial measurement noise covariance on the SOC estimation

Initial measurement noise covariance is also an important parameter that affects the SOC estimation based on the IAUKF method. The effect of initial measurement noise covariance on the SOC estimation is also analysed, as shown in Fig. 18. Fig. 18(a) indicates that the proposed IAUKF is robust to initial measurement noise covariance. The local enlarged drawing in Fig. 18(a) shows that the estimated SOC under different initial measurement noise covariance converges to the reference SOC quickly with the time. Fig. 18(b) shows that the SOC error is close to zero although the initial measurement noise covariance is different.

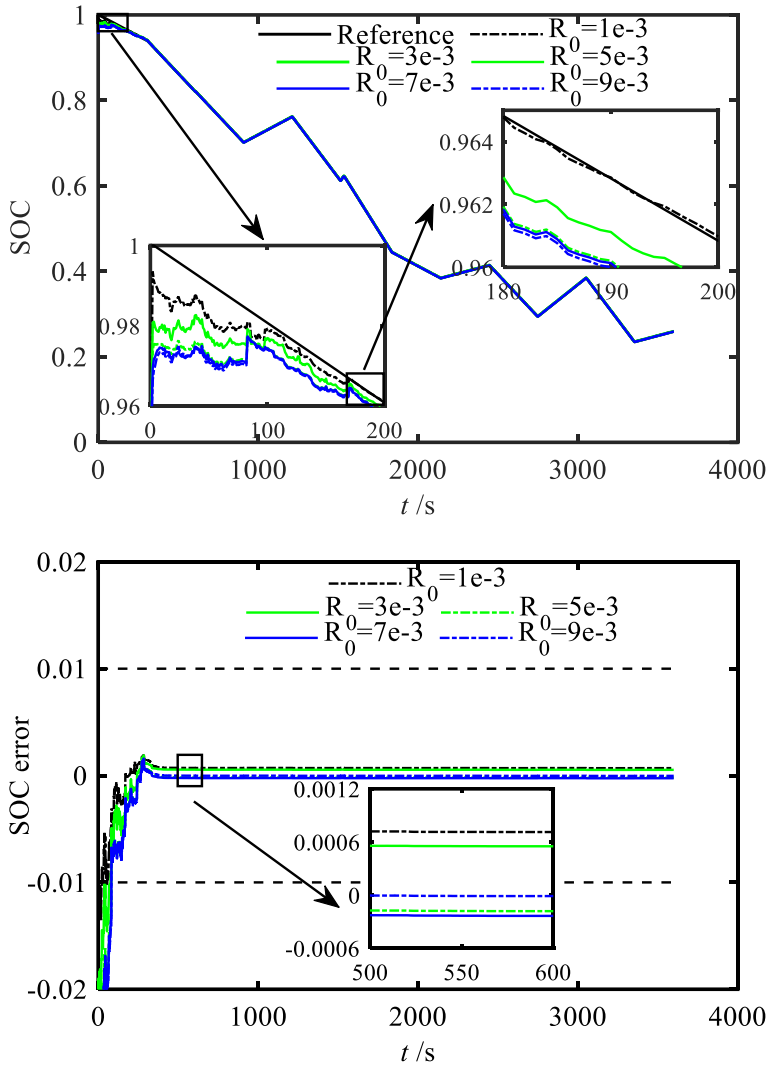

Fig. 18. The effect of $\mathbf{R}_0$ on (a) SOC and (b) its error

The corresponding RMSE and MAE of SOC are listed in Table 16. It can be found that the maximum RMSE of SOC is almost twice the size of the minimum one. The maximum MAE of SOC is 28.77% larger than the minimum one. The reason is that the initial measurement noise covariance significantly affects the convergence process at the time interval [0, 200]s, as shown in the local enlarged drawing in Fig. 18(a). However, under all cases, the SOC error tends to zero with the time although the initial measurement noise covariance is different. This is because the proposed online adaption algorithm gradually corrects the initial covariance estimation error. Therefore, the proposed IAUKF method is robust to the initial measurement noise covariance.

Table 16. RMSE and MAE under different initial measurement noise covariance

IAUKF	$\mathbf{R}_0$=1e-3	$\mathbf{R}_0$=3e-3	$\mathbf{R}_0$ = 5e-3	$\mathbf{R}_0$=7e-3	$\mathbf{R}_0$=9e-3
RMSE of SOC	0.00164	0.00248	0.00316	0.00335	0.00344
MAE of SOC	0.00094	0.00099	0.00083	0.00091	0.00073

To summarize, the minimum RMSE and MAE of SOC usually occur at different parameters. The RMSE of SOC is mainly determined by the initial convergence process. The MAE of SOC reflects the stable error of SOC, which should be put more emphasize on. Therefore, in order to obtain minimum MAE of SOC, the initial length L_0, threshold Th and initial measurement noise covariance should be set to 6, 4.5 and 5e-3 respectively.

5 Conclusions

AUKF has been widely used for battery SOC estimation based on ECM, and the accurate estimation of the ICM based on the EIS is key to the AUKF performance. To address the issue of the distribution change of EIS caused by load current dynamics and battery model error of AUKF, an IAUKF method is proposed as a way of improving the SOC estimation accuracy of LIBs. The following are conclusions drawn from this work:

(1) Compared to AUKF, IAUKF leads to 43.70% and 72.37% improvement in the estimation accuracy of RMSE and MAE of SOC under random walk discharge condition, respectively. The steady-state SOC error based on the proposed IAUKF method is very close to zero, which is significantly lower than the one based on the AUKF method.

(2) The computation time of the proposed IAUKF method only slightly increases by 6.27% compared with the one based on the AUKF method. Therefore, the proposed IAUKF method can be used for online SOC estimation.

(3) The effect of the initial length of the EIS on SOC results based on the IAUKF method is analysed. The initial length of the EIS affects the SOC accuracy indirectly by influencing the ICM

estimation. The result indicates that choosing proper initial window length of the EIS can further improve the SOC accuracy based on the proposed IAUKF method.

(4) The effect of the detection threshold for EIS distribution change on SOC results based on IAUKF method is analysed. The results indicate that selecting a proper threshold can further improve the SOC accuracy based on the proposed IAUKF method.

(5) The influence of initial measurement noise covariance on SOC results based on IAUKF method is analysed. The initial measurement noise covariance significantly affects the convergence process. However, the effect of the initial measurement noise covariance on the steady-state SOC error is negligible. The results indicate that the proposed IAUKF method is robust to initial measurement noise covariance.

In the short term, the influence of ageing on SOC estimation of lithium-ion battery is not significant, however, in the long term such influence can't be ignored. As the battery ages, the capacity of LIBs will change, which would also contribute to the distribution change of the EIS in the AUKF method. In the future, the capacity fade of LIBs will be taken into consideration in the proposed IAUKF method to further improve the online SOC accuracy in the long term.

Acknowledgements

The authors would like to thank the random walk discharge data provided by NASA Ames Prognostics Center from https://ti.arc.nasa.gov/tech/dash/groups/pcoe/prognostic-data-repository/, and the discharge data under DST and FUDS conditions provided by CACLE of Maryland University from https://web.calce.umd.edu/batteries/data.htm. The work has received support from the UK-China Joint Research and Innovation Partnership fund from China Scholarship Council (CSC) and British Council (BC) under the grant number 201703780098 and the grants from the National

Natural Science Foundation of China under grant number No. 51806189 and No. 51476143. The authors also would like to thank the supports from NSFC-RS Joint Project under the grant number No. 5151101443 and IE/151256. The support from Cao Guang Biao High Tech Talent Fund, Zhejiang University is also highly acknowledged. This work also received support from EPSRC for project TRENDS (reference number EP/R020973/1).

References

[1] Peng J, Luo J, He H, Lu B. An improved state of charge estimation method based on cubature Kalman filter for lithium-ion batteries. Applied Energy. 2019;253.
[2] Lyu Z, Gao R. A model-based and data-driven joint method for state-of-health estimation of lithium-ion battery in electric vehicles. International Journal of Energy Research. 2019;43:7956-69.
[3] Li D, Ouyang J, Li H, Wan J. State of charge estimation for LiMn2O4 power battery based on strong tracking sigma point Kalman filter. Journal of Power Sources. 2015;279:439-49.
[4] Tong S, Klein MP, Park JW. On-line optimization of battery open circuit voltage for improved state-of-charge and state-of-health estimation. Journal of Power Sources. 2015;293:416-28.
[5] Li Y, Wang C, Gong J. A multi-model probability SOC fusion estimation approach using an improved adaptive unscented Kalman filter technique. Energy. 2017;141:1402-15.
[6] Yang N, Zhang X, Li G. State of charge estimation for pulse discharge of a LiFePO4 battery by a revised Ah counting. Electrochimica Acta. 2015;151:63-71.
[7] Sun F, Xiong R, He H. A systematic state-of-charge estimation framework for multi-cell battery pack in electric vehicles using bias correction technique. Applied Energy. 2016;162:1399-409.
[8] Yang R, Xiong R, He H, Mu H, Wang C. A novel method on estimating the degradation and state of charge of lithium-ion batteries used for electrical vehicles. Applied Energy. 2017;207:336-45.
[9] Zheng F, Xing Y, Jiang J, Sun B, Kim J, Pecht M. Influence of different open circuit voltage tests on state of charge online estimation for lithium-ion batteries. Applied Energy. 2016;183:513-25.
[10] Yang F, Li W, Li C, Miao Q. State-of-charge estimation of lithium-ion batteries based on gated recurrent neural network. Energy. 2019;175:66-75.
[11] Chemali E, Kollmeyer PJ, Preindl M, Emadi A. State-of-charge estimation of Li-ion batteries using deep neural networks: A machine learning approach. Journal of Power Sources. 2018;400:242-55.
[12] Zhang C, Zhu Y, Dong G, Wei J. Data-driven lithium-ion battery states estimation using neural networks and particle filtering. International Journal of Energy Research. 2019;43:8230-41.
[13] Bian C, He H, Yang S. Stacked bidirectional long short-term memory networks for state-of-charge estimation of lithium-ion batteries. Energy. 2020;191:116538.
[14] Hu JN, Hu JJ, Lin HB, Li XP, Jiang CL, Qiu XH, et al. State-of-charge estimation for battery management system using optimized support vector machine for regression. Journal of Power Sources. 2014;269:682-93.
[15] Zahid T, Xu K, Li W, Li C, Li H. State of charge estimation for electric vehicle power battery using advanced machine learning algorithm under diversified drive cycles. Energy. 2018;162:871-82.
[16] Tang X, Gao F, Zou C, Yao K, Hu W, Wik T. Load-responsive model switching estimation for state of charge of lithium-ion batteries. Applied Energy. 2019;238:423-34.
[17] Pang H, Guo L, Wu L, Jin X. An enhanced temperature-dependent model and state-of-charge estimation for a Li-Ion battery using extended Kalman filter. International Journal of Energy Research. 2020;n/a.
[18] Jiang B, Dai H, Wei X, Xu T. Joint estimation of lithium-ion battery state of charge and capacity within an adaptive variable multi-timescale framework considering current measurement offset. Applied Energy. 2019;253.
[19] Wang S-L, Fernandez C, Zou C-Y, Yu C-M, Chen L, Zhang L. A comprehensive working state monitoring method for power battery packs considering state of balance and aging correction. Energy. 2019;171:444-55.
[20] Chen Z, Sun H, Dong G, Wei J, Wu J. Particle filter-based state-of-charge estimation and remaining-dischargeable-time prediction method for lithium-ion batteries. Journal of Power Sources. 2019;414:158-66.

[21] Wang Y, Zhang C, Chen Z. A method for state-of-charge estimation of Li-ion batteries based on multi-model switching strategy. Applied Energy. 2015;137:427-34.
[22] Lin Y, Xu X, Wang F, Xu Q. Active equalization control strategy of Li-ion battery based on state of charge estimation of an electrochemical-thermal coupling model. International Journal of Energy Research. 2020;44:3778-89.
[23] Meng J, Ricco M, Acharya AB, Luo G, Swierczynski M, Stroe D-I, et al. Low-complexity online estimation for LiFePO4 battery state of charge in electric vehicles. Journal of Power Sources. 2018;395:280-8.
[24] Peng J, Luo J, He H, Lu B. An improved state of charge estimation method based on cubature Kalman filter for lithium-ion batteries. Applied Energy. 2019;253:113520.
[25] Ren H, Zhao Y, Chen S, Yang L. A comparative study of lumped equivalent circuit models of a lithium battery for state of charge prediction. International Journal of Energy Research. 2019;43:7306-15.
[26] Weng C, Sun J, Peng H. A unified open-circuit-voltage model of lithium-ion batteries for state-of-charge estimation and state-of-health monitoring. Journal of Power Sources. 2014;258:228-37.
[27] Shen P, Ouyang M, Lu L, Li J, Feng X. The Co-estimation of State of Charge, State of Health, and State of Function for Lithium-Ion Batteries in Electric Vehicles. IEEE Transactions on Vehicular Technology. 2018;67:92-103.
[28] Ye M, Guo H, Cao B. A model-based adaptive state of charge estimator for a lithium-ion battery using an improved adaptive particle filter. Applied Energy. 2017;190:740-8.
[29] Shen Y. Adaptive extended Kalman filter based state of charge determination for lithium-ion batteries. Electrochimica Acta. 2018;283:1432-40.
[30] Li S, Hu M, Li Y, Gong C. Fractional-order modeling and SOC estimation of lithium-ion battery considering capacity loss. International Journal of Energy Research. 2019;43:417-29.
[31] Liu X, He Y, Zheng X, Zhang J, Zeng G. A new state-of-charge estimation method for electric vehicle lithium-ion batteries based on multiple input parameter fitting model. International Journal of Energy Research. 2017;41:1265-76.
[32] Hu X, Jiang H, Feng F, Liu B. An enhanced multi-state estimation hierarchy for advanced lithium-ion battery management. Applied Energy. 2020;257:114019.
[33] Li Y, Wang C, Gong J. A wavelet transform-adaptive unscented Kalman filter approach for state of charge estimation of LiFePo4 battery. International Journal of Energy Research. 2018;42:587-600.
[34] Wang T, Chen S, Ren H, Zhao Y. Model-based unscented Kalman filter observer design for lithium-ion battery state of charge estimation. International Journal of Energy Research. 2018;42:1603-14.
[35] Linghu J, Kang L, Liu M, Luo X, Feng Y, Lu C. Estimation for state-of-charge of lithium-ion battery based on an adaptive high-degree cubature Kalman filter. Energy. 2019;189:116204.
[36] Cui X, He Z, Li E, Cheng A, Luo M, Guo Y. State-of-charge estimation of power lithium-ion batteries based on an embedded micro control unit using a square root cubature Kalman filter at various ambient temperatures. International Journal of Energy Research. 2019;43:3561-77.
[37] Campestrini C, Heil T, Kosch S, Jossen A. A comparative study and review of different Kalman filters by applying an enhanced validation method. Journal of Energy Storage. 2016;8:142-59.
[38] Shu X, Li G, Shen J, Yan W, Chen Z, Liu Y. An adaptive fusion estimation algorithm for state of charge of lithium-ion batteries considering wide operating temperature and degradation. Journal of Power Sources. 2020;462:228132.
[39] Wang L, Lu D, Liu Q, Liu L, Zhao X. State of charge estimation for LiFePO4 battery via dual extended kalman filter and charging voltage curve. Electrochimica Acta. 2019;296:1009-17.
[40] Guo F, Hu G, Zhou P, Hu J, Sai Y. State of charge estimation in electric vehicles at various ambient temperatures. International Journal of Energy Research. 2020;n/a.
[41] Wang Q, Kang J, Tan Z, Luo M. An online method to simultaneously identify the parameters and estimate states for lithium ion batteries. Electrochimica Acta. 2018;289:376-88.
[42] Hou J, Yang Y, Gao T. A normal-gamma-based adaptive dual unscented Kalman filter for battery parameters and state-of-charge estimation with heavy-tailed measurement noise. International Journal of Energy Research. 2020;44:3510-25.
[43] Xiong R, Yu Q, Wang LY, Lin C. A novel method to obtain the open circuit voltage for the state of charge of lithium ion batteries in electric vehicles by using H infinity filter. Applied Energy. 2017;207:346-53.
[44] Jiang B, Dai H, Wei X, Xu T. Joint estimation of lithium-ion battery state of charge and capacity within an adaptive variable multi-timescale framework considering current measurement offset. Applied Energy. 2019;253:113619.
[45] Ye M, Guo H, Xiong R, Yu Q. A double-scale and adaptive particle filter-based online parameter and state of charge estimation method for lithium-ion batteries. Energy. 2018;144:789-99.
[46] Lai X, Zheng Y, Sun T. A comparative study of different equivalent circuit models for estimating state-of-charge of lithium-ion batteries. Electrochimica Acta. 2018;259:566-77.

[47] Xiong R, Sun F, Gong X, Gao C. A data-driven based adaptive state of charge estimator of lithium-ion polymer battery used in electric vehicles. Applied Energy. 2014;113:1421-33.
[48] Sun F, Hu X, Zou Y, Li S. Adaptive unscented Kalman filtering for state of charge estimation of a lithium-ion battery for electric vehicles. Energy. 2011;36:3531-40.
[49] Bole BK, C.S.; Daigle, M. Adaptation of an Electrochemistry-based Li-Ion Battery Model to Account for Deterioration Observed Under Randomized Use. In Proceedings of the Annual Conference of the Prognostics and Health Management Society. Fort Worth, TX, USA2014.
[50] Andersson J. Lifetime estimation of Lithium-ion batteries for stationary energy storage systems. Stockholm: KTH Royal Institute of Technology; 2017.